Department of Physics and Astronomy

University of Heidelberg

Master thesis

in Physics

submitted by

B.Sc. Felix Nüßlein

born in Gunzenhausen (Germany)

2018

# An experimental setup for testing ion beam sources

# for

# the CSR facility

This Master thesis has been carried out by Felix Nüßlein

at the

Max-Planck-Institut für Kernphysik in Heidelberg

under the supervision of

Prof. Andreas Wolf

**Ein experimenteller Aufbau zum Testen von Ionenstrahl-Quellen für die CSR-Anlage**

Der tiefkalte Speicherring (CSR) in Heidelberg gehört zur neuen Generation der elektrostatischen Ionen-Speicherringe. Seine experimentellen Vakuumkammern werden auf eine Temperatur von 6 K heruntergekühlt, was zu Restgasdichten $< 140$ cm$^{-3}$ führt und die Speicherung schneller Ionenstrahlen (bis zu 300 keV/u) bis zu Stunden ermöglicht. Das kalte Strahlungsfeld und die masseunabhängige Speicherung über lange Zeitskalen erlauben es Forschern, die Stabilität, Wechselwirkungen und spektroskopischen Eigenschaften einer großen Vielfalt an Atom-, Molekül- und Clusterionen zu untersuchen.
Daher wird die 300-keV-Quellenplattform der CSR-Anlage voraussichtlich verschiedene Ionenquellen beherberbergen, die Ionenstrahlen von leichten und schweren Atomen, Molekülen, Clustern und Biomolekülen für den CSR bereitstellen.
Um diese Quellen (insbesondere eine neue Laserverdampfungsquelle zur Erzeugung kalter $(SF_6)_N^-$-Cluster) zu testen und ihre Produktionsleistung unabhängig von der CSR-Anlage zu optimieren, wird *in dieser Arbeit* ein magnetisches Massenspektrometer entworfen, aufgebaut und mit einer Penning-Ionenquelle charakterisiert. Zusätzlich wird eine Methode entwickelt, um ohne den exakten Wert des magnetischen Krümmungsradius das effektive elektrische Potential $U'$, auf dem Ionen in der Quelle geboren werden, präzise ($\leq 0.2\%$) zu bestimmen.

**An experimental setup for testing ion beam sources for the CSR facility**

The Cryogenic Storage Ring (CSR) in Heidelberg is a next-generation electrostatic ion storage ring. Its experimental vacuum chambers are cooled down to a temperature of 6 K, leading to residual gas densities of $< 140$ cm$^{-3}$ and to storage times of fast ion beams (up to 300 keV/u) on the order of hours. The cold radiative environment and the mass-independent storage over long time scales give access to the study of the stability, spectroscopic properties and interactions for a great variety of atomic, molecular and cluster ions.
Several ion sources are foreseen to be operated on the 300 keV acceleration platform of the CSR facility in order to produce a wide range of ion beams from light and heavy atoms, molecules, clusters and biomolecules.
For the purpose of testing those sources (especially a new Laser VAPorization source producing cool $(SF_6)_N^-$ clusters) and of optimizing their output independently of the CSR facility, a magnetic mass spectrometer is designed, set up and characterized with a Penning ion source *in this thesis*. Additionally, a method for precisely ($\leq$ 0.2%) determining the effective electrical potential $U'$ at which ions are born inside the Penning source without prior knowledge of the exact magnetic bending radius is developed.

# Contents

## List of acronyms

| | |
|---|---|
| **BIRD** | Blackbody-Induced Radiative Dissociation |
| **CFD** | Constant Fraction Discriminator |
| **CSR** | Cryogenic Storage Ring |
| **CTF** | Cryogenic Trap for Fast ion beams |
| **EIBT** | Electrostatic Ion Beam Trap |
| **ESI** | Electrospray Ionization |
| **FWHM** | Full Width at Half Maximum |
| **LVAP** | Laser VAPorization |
| **MISS** | Metal Ion Sputter Source |
| **MPIK** | Max-Planck-Institut für Kernphysik |
| **ODR** | Orthogonal Distance Regression |
| **RFQ** | Radio-Frequency Quadrupole |

# 1 Ion sources and experimental projects for the CSR

## 1.1 The CSR facility

In the last few years, a new generation of electrostatic cryogenic storage rings [16, 28, 34] has been put into operation. The unique combination of their properties greatly widens the scope for gas-phase experiments performed on atomic and molecular ion beams. For example, such devices can store light and heavy atomic ions as well as ions of large biomolecules and heavy clusters with kinetic energies in the keV range. The experimental vacuum chambers of those devices are cooled down to temperatures of 10 K or lower which was shown to lead to residual gas densities as low as 140 $cm^{-1}$ [16]. The long storage times of up to hours allow researchers to study slow physical processes, e.g., rotational cooling processes in the interstellar space [30, 23, 33], the spontaneous fragmentation of metal cluster ions [1, 17] or the decay of excited anionic states via dipole-forbidden transitions [7]. It was demonstrated [23] that such storage devices provide a cold radiative environment. This observation enables studies of van der Waals clusters which quickly dissociate due to the absorption of blackbody radiation in a room temperature experiment.

The Cryogenic Storage Ring (CSR) at the Max-Planck-Institut für Kernphysik (MPIK) in Heidelberg is a cryogenic electrostatic storage ring suited for ion beams in a wide energy range (up to 300 keV) allowing also merged beams operation and phase space cooling. The closed ion orbit of the CSR has a circumference of about 35 m and the fourfold symmetry of its ion-optical design provides four (red in figure 1) almost field-free linear sections with a length of about 2 m each. In those sections the stored ion beam can interact with beams of neutrals, photons or cold electrons.

Apart from the storage ring itself, the CSR facility comprises two ion source plat-

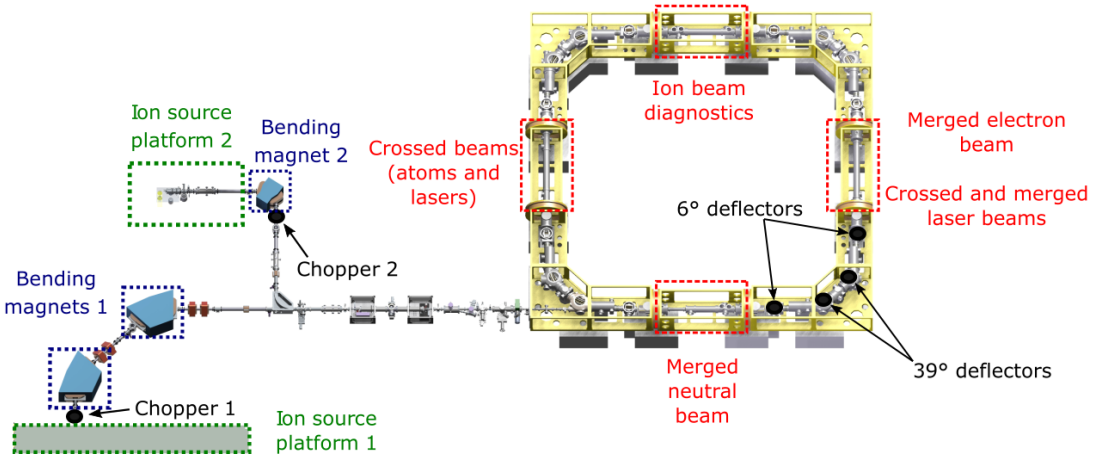


Figure 1: A sketch of the CSR facility. Each corner of the CSR houses two 39° and two 6° deflectors. Adapted from [35].

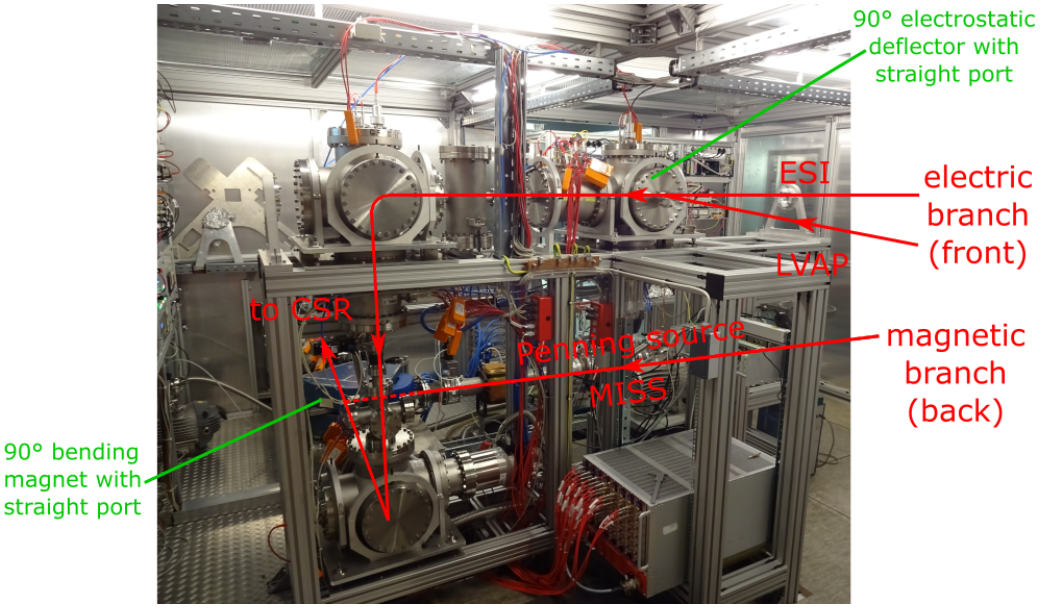


Figure 2: The current status of the 300 keV source platform of the CSR facility. The ESI source and the LVAP source are foreseen for the fully electrostatic part of the source platform. Red arrows indicate the ion trajectory. The Penning ion source and the MISS use the 90° port of the bending magnet and are not visible in the photograph. After the 90° bending magnet, the ions are accelerated and transported to the CSR.

forms (green in figure 1), where the ion beams for the experiments are produced and accelerated to kinetic energies of up to 300 keV (platform 1) or 60 keV (platform 2) per unit charge. The beam component with the desired mass-to-charge ratio is selected with bending magnets (blue in figure 1) and injected into the CSR. Additionally, the beam is chopped (chopper 1 and 2) in order to fill a controlled fraction of the ring with ions.

## 1.2 Ion sources for the CSR facility

The variety of atomic, molecular and cluster ions which will be studied at the CSR facility is produced by different types of ion sources. The 300 keV source platform [27] (see figure 2) is designed to house a Heinicke-type Penning ion source [18] for positive ions, a Middleton-type Metal Ion Sputter Source (MISS) for negative ions, a Laser VAPorization (LVAP) ion source for the production of clusters and an Electrospray Ionization (ESI) source, mainly intended for organic molecules.

Of these ion sources, the Penning source produces µA currents of positive ions from a gas discharge [38]. The choice of the carrier gas determines the ion species, e.g., $Ar^+$ or $N_2^+$. One can also use gas mixtures in order to create molecular ions

composed of more than one element. The Penning ion source has a compact size and is quite user-friendly compared to other ion sources. It is therefore well suited for testing new beamlines.

In a MISS, a solid surface is sputtered with positively charged cesium ions in order to create negative ions from the surface material [25], which are either used directly or as electron donor for particles entering the source by a gas. As demonstrated in [26], this source can produce a great variety of negative ions of atoms or molecules, ranging from $H^-$ to $PbO_2^-$, for example. The obtained ion beam currents are typically in the µA range.

With an ESI source droplets of a solvent containing the molecules of interest are injected into the vacuum. The molecules are ionized while they are inside the droplets. The solvent evaporates and the ions remain. This ionization process is considered to be very gentle since the molecules stay intact [14]. An ESI source produces ion currents between 10 fA [10] and 100 pA [22]. Due to the low intensity the desired ion species has to be accumulated—for example in a Radio-Frequency Quadrupole (RFQ) trap—prior to injection into the ring.

In an LVAP source [24] a plasma is created by ablating a metal target with a pulsed laser. The plasma contains free metal ions and electrons. A carrier gas with a pressure of up to 20 bar is pulsed into a $10^{-4}$ mbar vacuum with a pulse duration of about 40 µs. Shortly after the laser pulse the plasma is flushed away by the carrier gas. As the carrier gas expands, it cools down and sympathetically cools the metal plasma. Positively and negatively charged metal cluster ions are created. Additionally, we can add other gases to the carrier gas. For example we can use $SF_6$ gas in order to produce negatively charged cluster from it. It was observed [5] that an LVAP produces cluster ions with low rovibrational energies. From the experiments performed with this source at the Cryogenic Trap for Fast ion beams (CTF) we expect that the produced amount of ions is sufficient for experiments at the CSR.

The 300 keV platform has a magnetic and an electric branch as shown in figure 2. So far, the CSR was operated using the magnetic branch with mainly the Penning and the MISS ion sources. On the other hand, the ESI and the LVAP source will be operated on the electric branch which is presently being commissioned.

## 1.3 Motivation and outline of this work

Recently, the Blackbody-Induced Radiative Dissociation (BIRD) [11] of van der Waals clusters was studied for $(SF_6)_N^-$ [31] and $SF_5^+(SF_6)_N$ [37] clusters which were stored in an Electrostatic Ion Beam Trap (EIBT) at room temperature. However, the stability of the clusters has not yet been examined for a strongly suppressed thermal background. We aim at storing $(SF_6)_N^-$ clusters in the CSR in order to study their ground state stability and their heating dynamics for various radiative

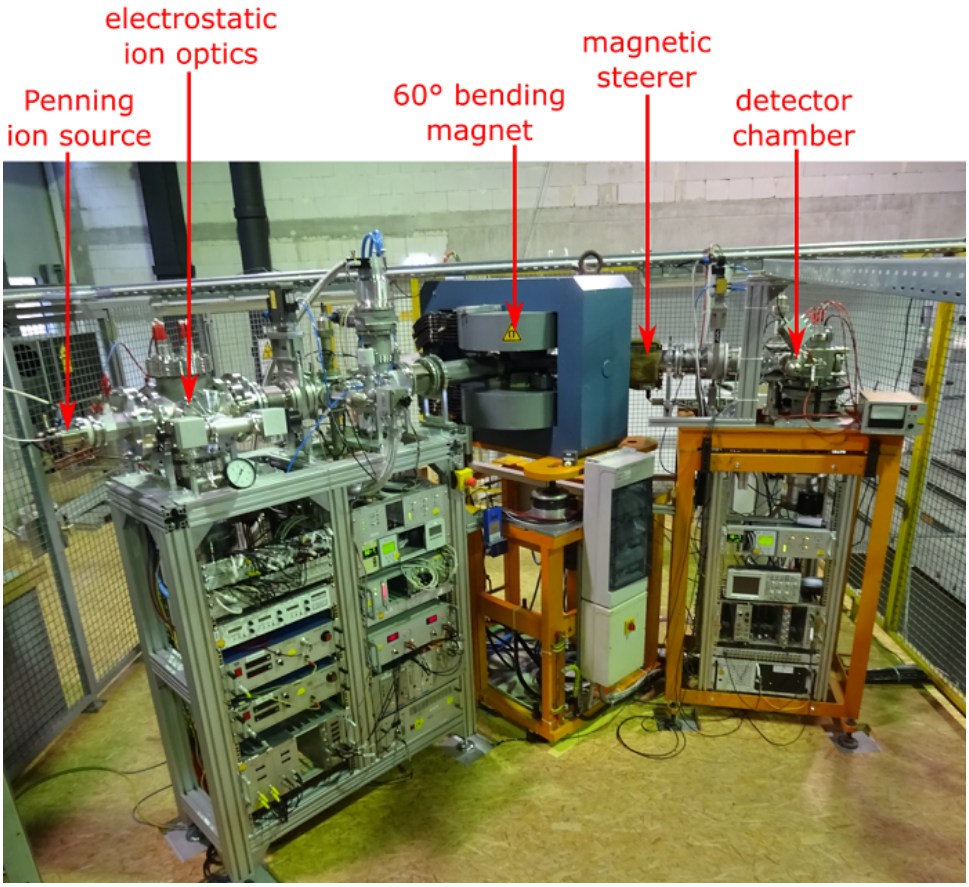


Figure 3: The setup for testing ion sources characterized in this work is presented.

environments. Currently, we are developing [29] a new LVAP source in order to produce cool $(SF_6)_N^-$ clusters for the CSR.

To test the LVAP source and to optimize the production of $(SF_6)_N^-$ clusters independent of the CSR facility it was decided to create an additional setup that essentially represents a magnetic mass spectrometer. In the course of the present work, such a setup (see figure 3) has been designed and taken into operation. It is based on a large 60° bending magnet to which a detector system with a Faraday cup and a channeltron, similar to a detector system used at the CSR facility, has been added. The source port of the setup with electrostatic steerers and an electrostatic einzel lens is designed to be as similar as possible to the LVAP source port at the electric branch of the 300 keV platform (see figure 2). In addition, we introduce a pick-up electrode for ion bunches. The setup is characterized with a Penning ion source, remaining compatible with other ion sources and in particluar the LVAP source to be employed in the BIRD studies mentioned above.

# 2 Experimental setup for testing ion beam sources

## 2.1 Overview

Our experimental setup consists of a magnetic mass spectrometer to which ion sources of various types can be coupled. The setup shown in figure 4 and 5 operates with pulsed and continuous ion beams under high vacuum conditions on the order of $10^{-7}$ mbar. It consists of an ion source which produces beams with kinetic energies up to 12.5 keV (in our case the Penning source), a magnet for mass analysis with a bending radius of about 0.3 m and a detector system for counting positive and negative ions and measuring ion beam currents down to 10 pA. Similar to the concept of a beamline used in [26] for extensive research of a MISS, horizontal slits are positioned in the focal points of the magnet in order to fit the trajectory of the ions to the bending radius of the magnet. In addition, pick-up electrodes for detecting microsecond-long ion bunches are located before and after the magnet. In the following the beamline section before the magnet, the magnet section and the section after the magnet will be referred to as sector I, II and III as shown in figure 4. More detailed views of sector I and III are presented in figure 5 (b) and (c).

The ion source is electrically isolated from the other components of the setup. An extraction voltage of up to 12.5 kV is applied to the ion source chamber while the rest of the vacuum chambers remains at ground potential. Ions with a mass-to-charge ratio $m/q$ and a potential energy

$$E_{el} = qU \tag{1}$$

are born in the ion source at an effective potential $U$ with respect to ground. The ions are extracted from the source and accelerated to the final velocity

$$v = \sqrt{\frac{2E_{kin}}{m}} = \sqrt{\frac{2qU}{m}}. \tag{2}$$

Here, we use conservation of energy $E_{el} = E_{kin}$. In the field of the 60° bending magnet with field lines perpendicular to the ion trajectory the ions experience the Lorentz force

$$F_l = qvB \tag{3}$$

where we assume that no electrical field is present. The Lorentz force counteracts the centrifugal force

$$F_c = \frac{mv^2}{r}. \tag{4}$$

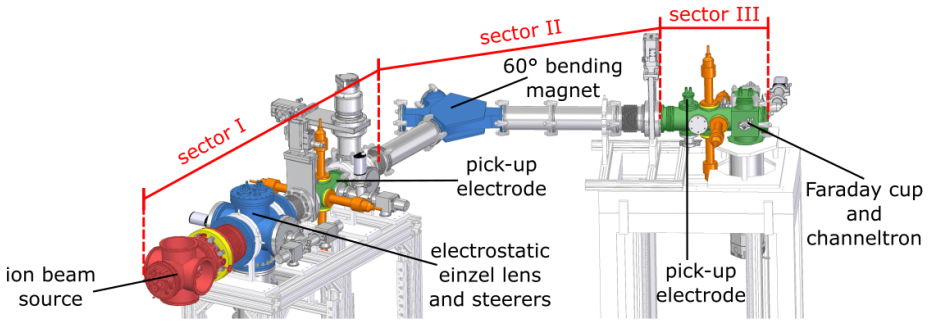


Figure 4: The experimental setup is comprised of chambers housing an ion source (red), ion optical elements (blue) and diagnostic elements (green).

The magnetic field $B$ thus separates the ions by their mass-to-charge-ratio

$$\frac{m}{q} = \frac{(Br)^2}{2U}, \tag{5}$$

considering a fixed voltage $U$ and a fixed bending radius $r = r_b$ [9].

After the ion beam is extracted from the source, two einzel lenses in sector I focus the ion beam in order to optimize the transmission of the beam through the bending magnet. The first einzel lens belongs to the Penning ion source and focuses the highly divergent beam shortly after extraction. The second einzel lens permanently remains in the CF chamber of the setup for ion sources without a dedicated focusing unit. Consequently, we refer to the components as einzel lens 1 and 2.

The ion beam is focused so that it has a minimum waist radius in the first focal point of the bending magnet. After transmission through the magnet it reaches a second beam waist. The focal points are located about 1 m before and after the pole shoe of the magnet. A beam offset can be corrected with two pairs of horizontal and vertical electrostatic steerers in sector I (see figure 5 (b)) and horizontal and vertical magnetic steerers directly after the magnet in sector II (see figure 3).

Horizontal slit pairs located at each of the two focal points of the magnet complete the mass spectrometer. The horizontal slit pair in sector I (see figure 5 (b)) defines the trajectory of the particles before they enter the magnet and cuts away unwanted spatial beam components. The horizontal slit pair in sector III selects the beam component with the desired mass-to-charge ratio and defines the resolution of the system. Additionally, two vertical slit pairs are used to spatially manipulate the beam without affecting the mass spectrometer.

Two pick-up electrodes in sector I and III detect pulsed beams (see figure 5 (b) and (c)). The detector system combining a Faraday cup and a channeltron at the end of the beamline measures the current of continuous ion beams down to an intensity of 10 pA and with suitable electronics counts ions up to a rate of $10^7$ $s^{-1}$.

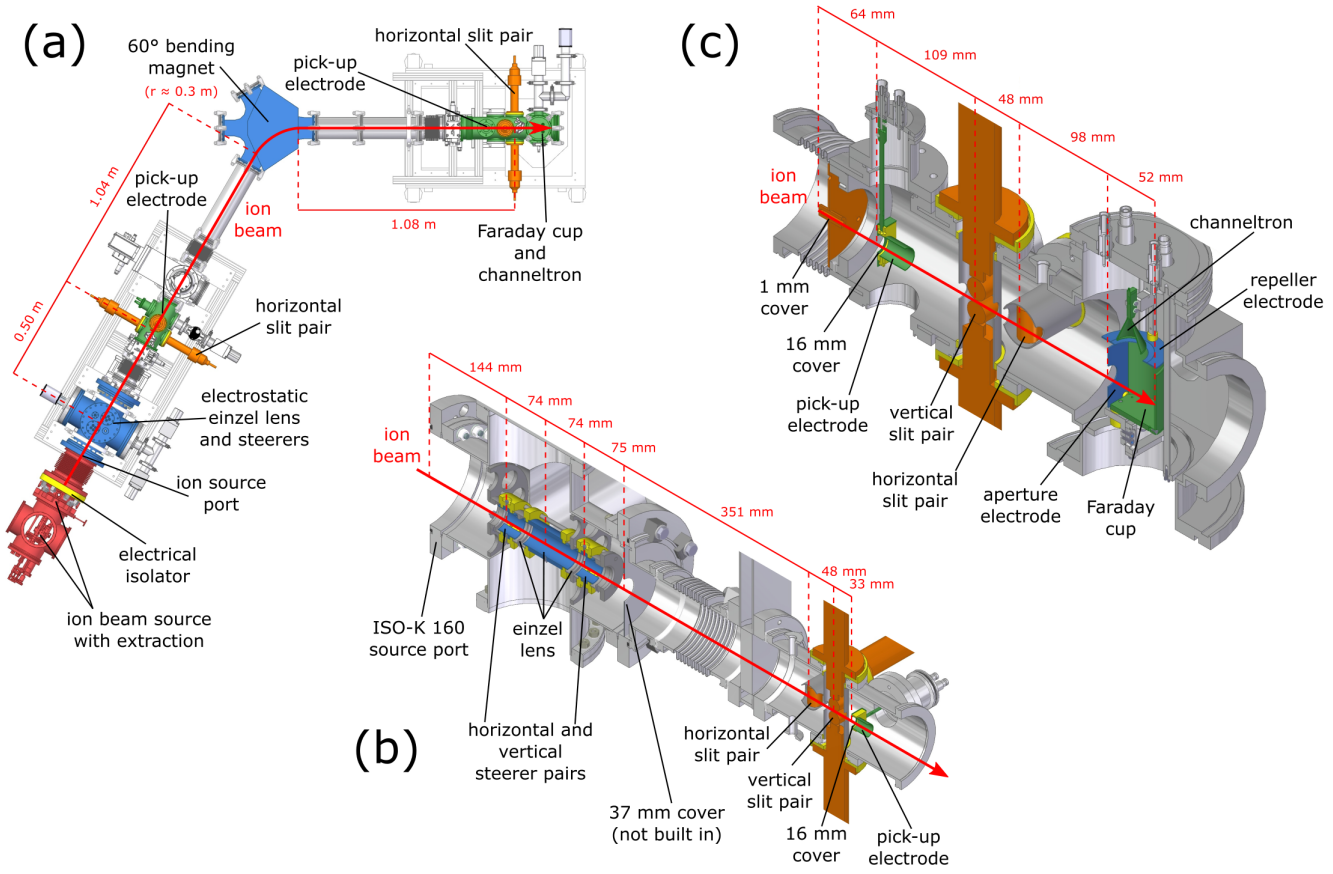


Figure 5: (a) Birdseye view of the experimental setup. The two horizontal slits (orange) are positioned approximately in the focal points of the magnet. (b) A detailed view of beamline sector I with electrostatic ion-optical elements (blue) and a pick-up electrode (green). Hammer-shaped slits (orange) housed in tantalum hulls manipulate the beam profile. (c) A detailed view of beamline sector III. The chamber houses diagnostic elements (green) for detecting pulsed and continuous ion beams. A 1 mm aperture (orange) is located directly after the bellows.

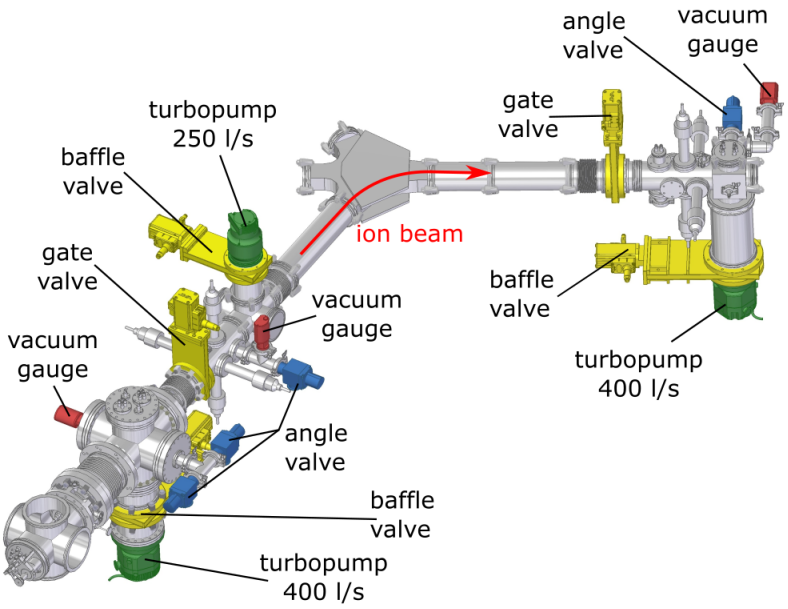


Figure 6: Vacuum system of the experimental setup. Two gate valves and three baffle valves (yellow) divide the vacuum system into three sections with independent pumping (green), vacuum measurement (red) and ventilation (blue).

## 2.2 Vacuum system

To minimize particle loss due to collisions with ambient gas during the transport from the source to the detector, vacuum conditions on the order of $10^{-6}$ mbar or better are needed. The vacuum system is shown in figure 6. Three turbo pumps and two scroll pumps are used to pump the chambers. Baffle valves protect the turbo pumps and two gate valves divide the vacuum system into three independent sections. The sections can be pumped and ventilated individually and each of the vacua is measured with a Penning vacuum gauge. The magnet and the detector chambers can thus remain pumped when the ion source is exchanged. The system uses the ISO-K chamber standard with O-ring seals except for the metal-sealed CF chamber with einzel lens 2 and the ion source port. The ion source is connected to the source port via an ISO-K 160 adapter which is permanently mounted at the CF chamber. In the idle state, a very good vacuum between $1 \times 10^{-7}$ mbar and $3 \times 10^{-7}$ mbar depending on the section is reached. The Penning ion source operates with gas pressures of 100–140 mbar in order to sustain the gas discharge. It is thus not surprising that the vacuum shortly behind the source is in the $10^{-5}$ mbar regime when the Penning ion source is active.

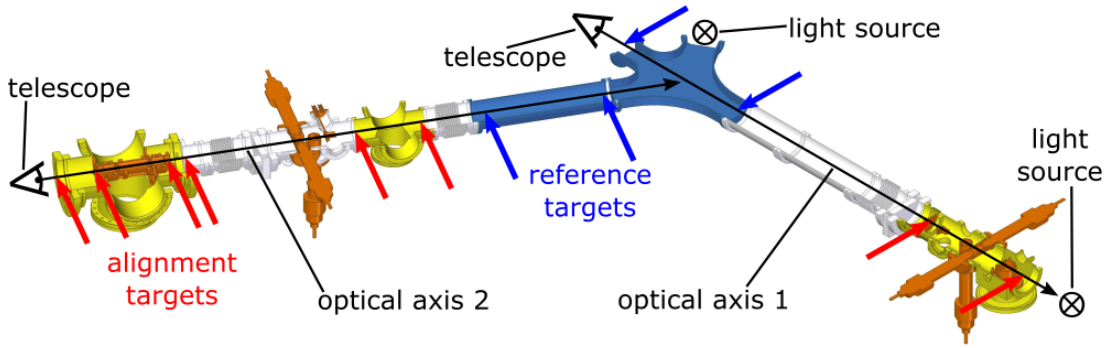


Figure 7: The vacuum chambers (yellow) and ion-optical components (orange) are aligned with a telescope and glass targets at the positions indicated by the red and blue arrows. The two reference axes are provided by the straight ports of the magnet and the tube attached to one of the 60° ports (blue).

## 2.3 Alignment of the chambers

The slits before and after the magnet define the trajectory of the particles and have to be aligned to the axes provided by the magnet chamber (see figure 7). We level the magnet horizontally and place bull's-eye targets at the flanges belonging to the two straight ports of the magnet chamber (blue arrows). We align the optical axis of a Taylor-Hobson telescope [16] to the axis defined by the target centers by using the telescope's cross hair. Then the bull's-eye targets are removed and placed at the flanges of the detector chamber (red arrows), which is then aligned to the optical axis. Similarly, the remaining components in sector III (orange) are aligned.

For the axis of sector I, the magnet chamber does not have an alignment port directly opposed to the 60° port. To provide a reference axis for the telescope in this sector, two bull's-eye targets are placed at both ends of the 420 mm steel tube attached to the magnet chamber (blue arrows). We then align the components in the same way as described for sector III. Red arrows indicate the position of bull's-eye targets. We estimate the relative precision $\delta_{rel}$ of the alignment method of sector I to

$$\delta_{rel} \leq \frac{\delta_{abs}}{d_t} = \frac{0.2 \text{ mm}}{400 \text{ mm}} = 5 \times 10^{-4}. \tag{6}$$

Here, $\delta_{abs}$ is the maximum possible radial displacement between the flanges of the steel tube given by the manufacturing precision and $d_t$ is the distance between the two targets. The ion source port (leftmost red arrow in figure 7) located about $D \approx 1.7$ m upstream of the 60° degree port can thus have a maximum radial displacement of $\Delta_{abs} \approx 0.85$ mm, which is an acceptable systematic shift for such a beamline. The shift can be corrected with the steerers.

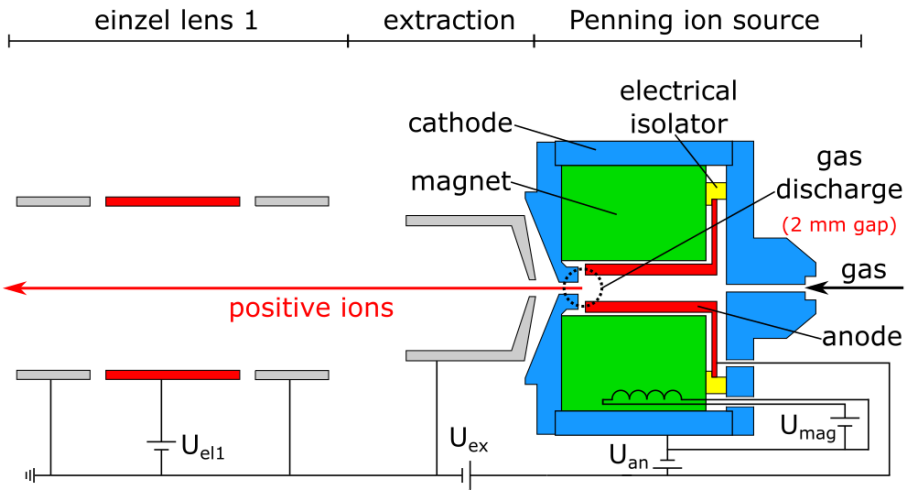


Figure 8: Schematic sectional view of the Penning ion source used for producing a positive ion beam with a gas discharge. In addition, the electrical circuitry is shown. The potential difference between the cathode (blue) and the anode (red) is on the order of 800 V. The loops of the magnet coil (green) wind around the anode cylinder. The magnetic field lines inside the coil are parallel to the symmetry axis of the Penning ion source. The einzel lens focusing the extracted ion beam belongs to the source (see figure 9).

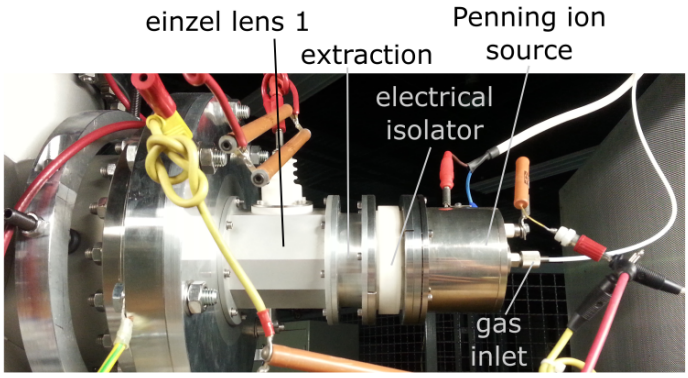


Figure 9: The Penning ion source including an electrical isolator, an extraction section and an einzel lens is mounted at the source port of the experimental setup. The shown resistors serve as load resistors for the power supplies. They are not shown in figure 8.

## 2.4 Ion production and acceleration

Any ion source can be mounted at the ion source port and has to bring its own extraction and acceleration systematics including an electrical isolator that separates the source potential from the ground potential of the setup. For example, the LVAP source discussed in section 1 utilizes a stepwise acceleration system in combination with differential pumping to extract the well-collimated beam as smoothly as possible. The highly divergent beam of the Penning source is accelerated in a singly step and has to be focused as early as possible. In this work, the experimental setup is characterized with a Penning ion source. A schematic sectional view of the ion source including the electrical circuitry is presented in figure 8. Figure 9 shows a photograph of the Penning ion source mounted at the source port.

The choice of the gas fed to the Penning ion source determines the ion species produced by the source. We use argon and nitrogen as carrier gases. For an anode voltage of $U_{an} \approx 1500$ V and a gas pressure inside the source of 100–140 mbar a gas discharge ignites in the 2 mm gap between the cathode and the anode. The carrier gas is ionized by impact with free electrons created in the gas discharge. A magnetic field confines the electrons axially so that they oscillate between the hollow anode and the two end electrodes on cathode potential (blue in figure 8). Thereby, the ionization rate of the carrier gas increases.

At the ignition voltage a current of $I_{an} \approx 1.6$ mA flows between cathode and anode. Due to heating of the source at this high current a permanent operation at this voltage is not recommended. Once the discharge has been ignited, the anode voltage can be lowered to 700–800 V depending on the gas. The anode current then reduces to $I_{an} = 0.25$–$0.6$ mA. The ion source output is observed to be higher for a lower anode voltage. Below an anode voltage $U_{an} \approx 700$ V for argon carrier gas and $U_{an} \approx 800$ V for nitrogen carrier gas, the beam output becomes unstable and the gas discharge extinguishes eventually.

Ions with charge $q$ that escape the Penning source through the opening in the downstream cathode see the full source potential $U_{ex}$ and are accelerated to the final energy $E_{kin} \in [q(U_{ex} - U_{an}), qU_{ex}]$. Due to the high anode voltage and the low ionization energy of the gas particles on the order of $E_{ion} \approx 15$ eV [20] it is not precisely known at which exact voltage $0\ \text{V} \leq U' \leq U_{an}$ most of the ions are produced and we write

$$E_{kin} = q(U_{ex} - U'). \tag{7}$$

The ion cone emerging from the source is focused by einzel lens 1 with a voltage $U_{el1} \approx 9$ kV for $U_{ex} = 12.5$ keV. The grounded cylinder-shaped electrode between the Penning ion source and einzel lens 1 shields the electrical field lines of the source. We choose the electrical circuitry (see figure 8) so that the maximum beam energy

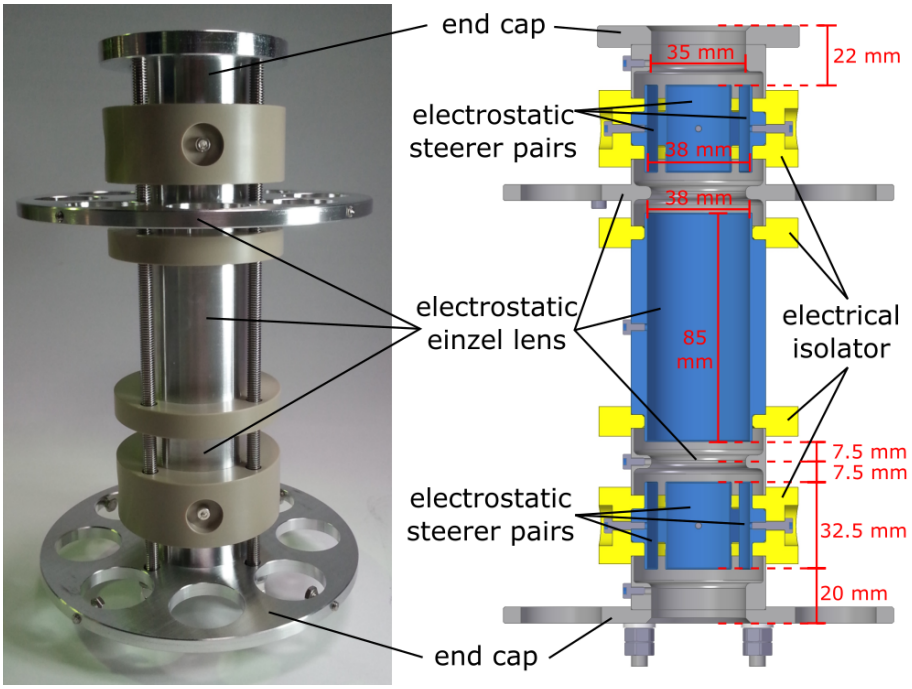


Figure 10: (a) A photograph and (b) a sectional view of the einzel lens steerer combination used in the experimental setup. Two pairs of horizontal and vertical steerers are arranged symmetrically around the einzel lens. The parts carrying voltage (blue) and the grounded parts (grey) screening the electrical field are separated by electrical isolators (yellow).

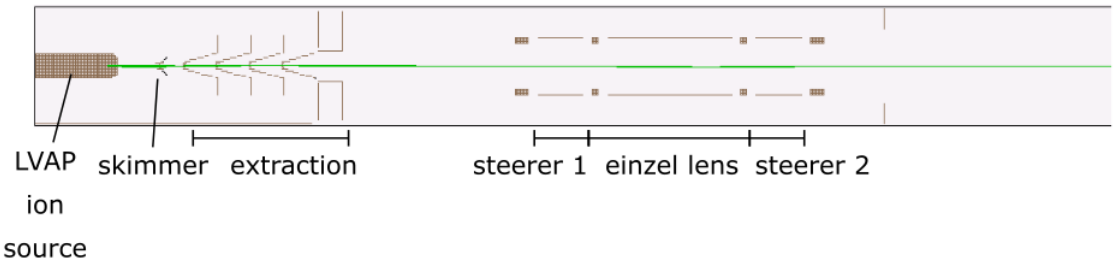


Figure 11: A simulation of a beam of singly charged positive ions with a beam energy of 5 keV in beamline sector I produced with an LVAP ion source is presented. The ion beam is focused and the trajectory is corrected by the einzel lens steerer combination (see figure 10) [36].

$$E_{kin,max} = qU_{ex} \tag{8}$$

is independent of the choice of the anode voltage $U_{an}$. The positive pole of the power supply providing the anode voltage is therefore connected to the extraction voltage $U_{ex}$.

## 2.5 Focusing and correction

The ion beam emerging from the source is further focused by einzel 2 in beamline sector I in order to optimize the transport of the beam through the magnet. Two horizontal and vertical steerer pairs located directly before and after einzel lens 2 correct a possible beam offset. The component combining this einzel lens and the steerer pairs is a modified version of a component used with a $C_{60}$ ion source at the Cryogenic Trap for Fast ion beams (CTF) [12]. It is shown in figure 10. A test of the dielectric strength shows that voltages of up to ±10 kV can be applied to the einzel lens. A steerer plate can hold voltages of up to ±2 kV.

To estimate the required voltages for the einzel lens and the steerer pairs, a SIMION simulation (see figure 11) of sector I was performed. In the simulation shown in figure 11 an LVAP produces a 5 keV beam of singly charged positive ions with a mass of 30 u. An initial beam profile with a rotationally symmetric Gaussian distribution with $\sigma = 0.05$ mm was assumed. To obtain a focal length of $f_{el} = 213$ mm, an einzel lens voltage of $U_{el} = 3130$ V is necessary. An initial beam offset of 0.25 mm was assumed and corrected with voltages of $U_{s1} = 30$ V and $U_{s2} = 20$ V applied at the first and second steerer pair. In the focal point the beam has a Gaussian distributed profile with $\sigma = 0.0265$ mm [36].

## 2.6 Mass selection

The 60° bending magnet ("Bruker B-E 33s") in beamline sector II separates the ion beam components by their mass-to-charge ratio. The magnet, the pole shoe and the Hall sensor measuring the magnetic flux density between the pole shoes are shown in figure 12. In figure 12 (b) we see that the magnetic field can not be measured directly below the ion trajectory. Instead, the Hall sensor is positioned as shown at a horizontal distance of about 5 cm from the ion trajectory.

In figure 12 (c) the position of the pole shoes (blue) relative to the magnet chamber is presented. The ion beam trajectory was geometrically determined (red line) by assuming that the magnetic field begins about $d = g/2 \approx 30$ mm [32] from the pole shoes, where $g = 61$ mm is the gap between the pole shoes. From the geometrical estimation we obtain a bending radius of $r_b = 0.300(9)$ m. The error results from the estimated uncertainty $\Delta d \approx 0.5$ mm of the range of the fringing field.

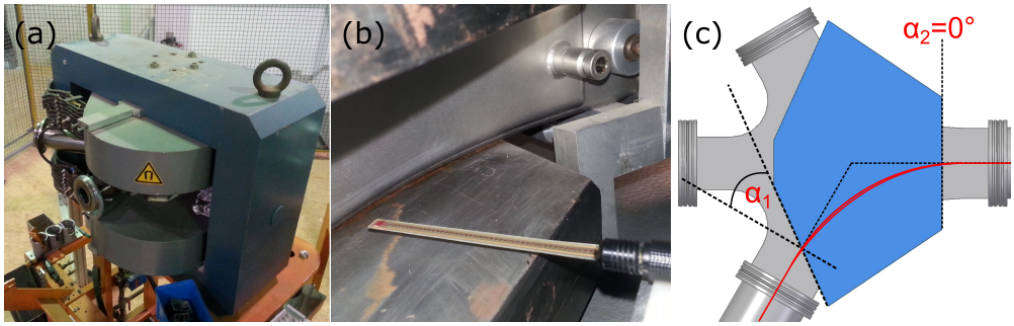


Figure 12: (a) A photograph of the magnet used for the mass spectrometer. (b) A photograph of the Hall sensor (red dot) without its protective cap measuring the magnetic field between the pole shoes at a distance of 5 cm from the ion trajectory. (c) A sketch of the upper pole shoe relative to the magnet chamber. The geometrically constructed ion trajectory (red) is shown. The linewidth represents the uncertainty of the bending radius.

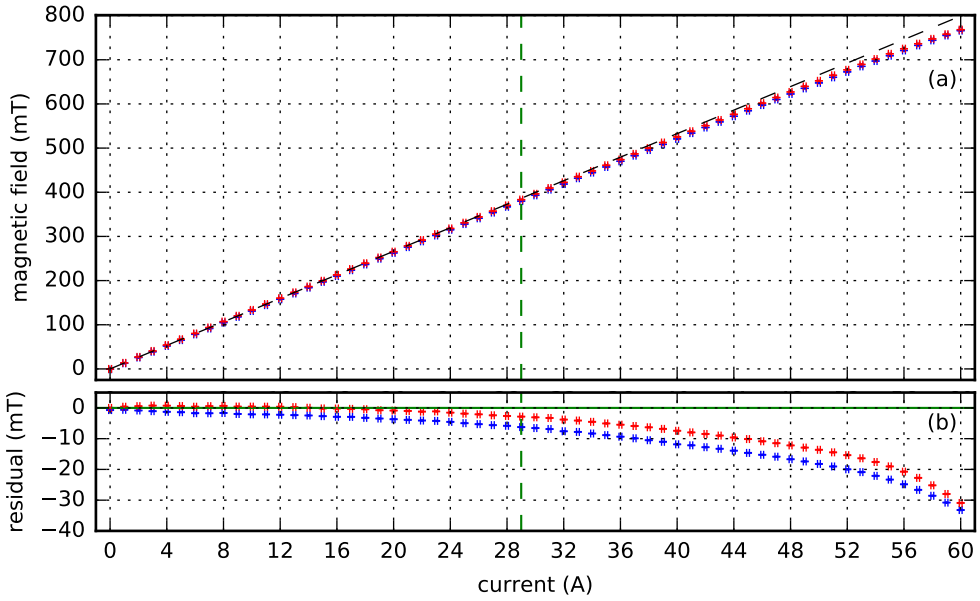


Figure 13: (a) A hysteresis curve of the magnet recorded for the Hall probe position as shown in figure 12 (b). The coil current was increased from 0 A to 60 A (blue data points) and decreased from 60 A to 0 A (red data points) in steps of 1 A. (b) The residuals result from fitting a line through the origin to the data points between 0 A and 29 A (vertical dashed line). An ODR fit algorithm [3] was used.

The hysteresis curve of the magnet is presented in figure 13. The measured magnetic field is plotted as a function of the coil current. Between 0 A and 25 A the magnetic field increases approximately linear with the coil current. Above a coil current of 25 A we observe saturation effects. For the maximum coil current of 60 A the average magnetic field is measured to be $B = 765.1(1.2)$ mT. With the bending radius of the magnet $r_b = 0.300(9)$ m and (5) we obtain that the 60° bending magnet can deflect ions with a mass-to-charge ratio up to

$$\left(\frac{m}{q}\right)_{max} = \frac{(Br)^2}{2U} = 1270(80)\ \frac{\mathrm{u}}{e} \tag{9}$$

at an estimated minimum value $U = 2$ kV for source operation.

The horizontal slits positioned in the focal points before and after the magnet determine the resolution of the mass spectrometer. In the following the position of the focal points will be estimated with a simulation of the magnet using MAD-X [15] and assuming an ion beam with a Gaussian distributed and radially symmetric beam profile with a standard deviation $\sigma = \sigma_x = \sigma_y$. The envelope

$$\sigma(s) \sim \sqrt{\epsilon\beta(s)} \tag{10}$$

of the beam at a position $s$ along its trajectory is obtained from the beam emittance $\epsilon$ and the betatron function $\beta(s)$. The beam emittance $\epsilon$ describes how well the ion beam is collimated and is therefore an indicator for the beam quality. An emittance on the order of $\epsilon = 5 \times 10^{-6}$ m rad or lower corresponds to a good beam quality. The betatron function $\beta(s)$ describes the transversal movement of the ions.

The vertical focusing properties of a deflecting magnet with a homogeneous field are defined by the pitch angles $\alpha_1$ and $\alpha_2$ between the transversal plane of the ion beam and the edges of the magnetic field (see figure 12 (c)). The gap $g$ between the pole shoes and the shape of their edges [19] also have an influence on the position of the focal points. Figure 14 shows a simulation of the 60° bending magnet for $g = 61$ mm, $\alpha_1 = 35.5°$ and $\alpha_2 = 0°$ and sharp perpendicular edges of the pole shoes [1]. The beam emittance and the initial betatron function were estimated to be $\epsilon = 30 \times 10^{-6}$ m rad and $\beta(s_1) = 0.3$ m/rad [32, 15]. We define the focal distances

$$f_1 = d_1 - d, \tag{11}$$
$$f_2 = d_2 - d \tag{12}$$

as the distances between the focal points and the edge of the magnetic field before ($f_1$) and after ($f_2$) the magnet. Here, $d_1$ and $d_2$ are the distances of the two focal

[1] The pole shoe edges are trimmed at a 45°×15 mm angle. A rough approximation with sharp rectangular edges was considered to be more reasonable than assuming Rogowski-shaped [4], smooth edges.

points from the edges of the pole shoes. The magnetic field is estimated to begin at a horizontal distance $d = g/2 \approx 30$ mm [32] from the edges of the pole shoes. From figure 14 we observe that if we choose a beam with a focus at $f_1 \approx 1$ m before the magnet, the resulting focus distance after the magnet is $f_2 \approx 1$ m for both the horizontal and the vertical axis of the beam profile. However, the horizontal and vertical standard deviation at the waist after the magnet differ from each other and from the initial value (see figure 14 (a)).

It was found that the choice of the initial betatron function $\beta(s_1)$ has an impact on the focal distance $f_2$ after the magnet. The initial betatron function is not known precisely and estimated to be in the interval $[0.1\ \text{m/rad}, 1.1\ \text{m/rad}]$ [13]. In figure 15 the horizontal and vertical focal distances after the magnet are simulated as a function of the focal distance $f_1$ before the magnet for various initial betatron functions in the interval. We observe that for longer focal distances $f_1$ the choice of the initial betatron function does have a smaller impact on the focal distances after the magnet. With this knowledge and due to the spatial constraints of the experimental site we position the horizontal slits at a distance $d_1 = 1.042(3)$ m before and at $d_2 = 1.080(2)$ m after the edges of the pole shoes (see figure 5 (a)).

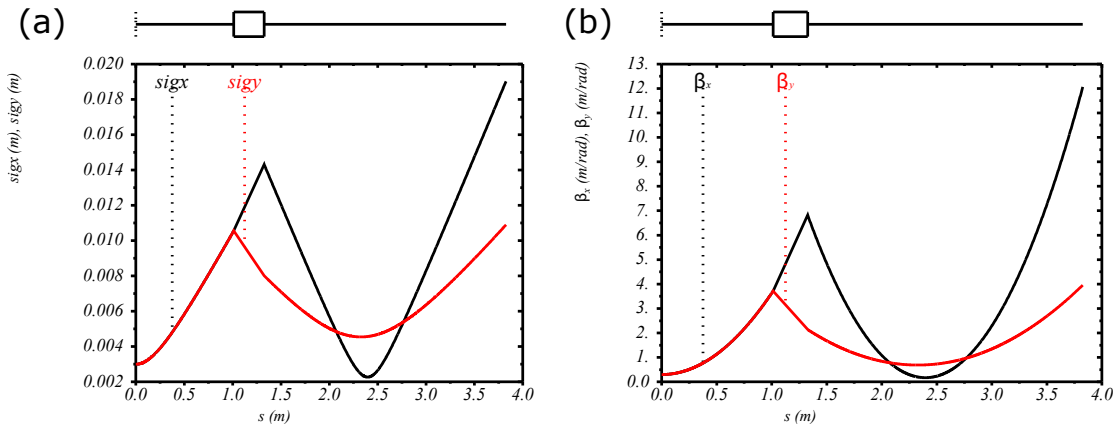


Figure 14: A simulation of the 60° bending magnet for $\beta(s_1) = 0.3$ m/rad, $\epsilon = 30 \times 10^{-6}$ m rad and a focal distance before the magnet of $f_1 = 1.012$ m. The beam has its first focal point at $s = 0$. (a) The horizontal (black) and vertical (red) beam envelope and (b) the horizontal (black) and vertical (red) betatron function $\beta(s)$ are plotted against the distance $s$ relative to the first focal point. The boxes in the upper part of the plots indicate the boundaries of the magnetic field including the fringing fields.

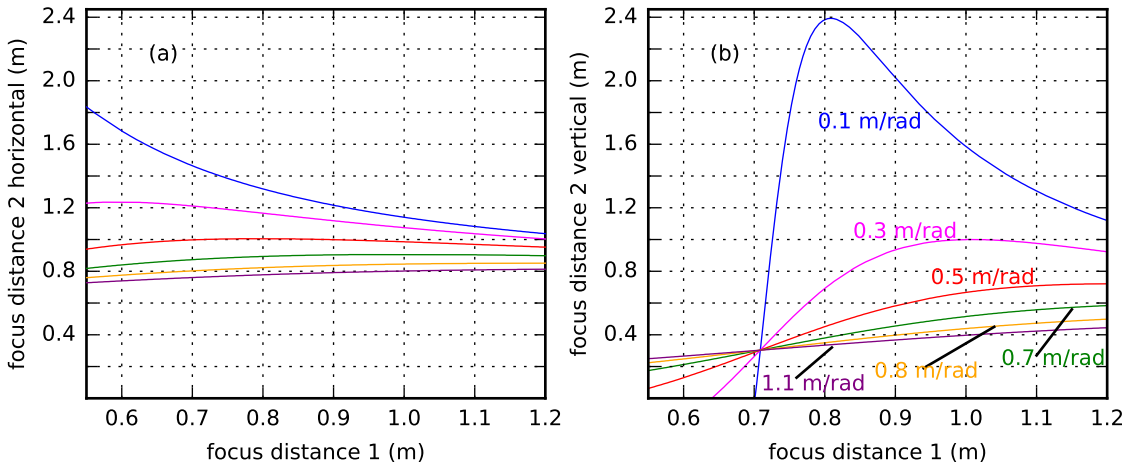


Figure 15: The horizontal (a) and vertical (b) focal distance after the magnet is plotted as a function of the focal distance $f_1$ before the magnet. We use the same colors in (a) and (b). The different curves result from different values of the initial betatron function $\beta$. We see that for longer focal distances $f_1$, the variation of the focal distances after the magnet for different values of $\beta(s_1)$ becomes smaller.

# 3 Methods for ion beam detection

## 3.1 Faraday cup and channeltron

In order to detect strong and weak ion beams with one detector system, a channeltron is combined with a Faraday cup. With a nanoamperemeter, ion beam currents down to 10 pA are measured at the Faraday cup. A channeltron counts single particles up to a rate of $10^7$ $s^{-1}$. Ion beam currents between 1.6 pA and 10 pA thus have an intensity too high for the channeltron and too low for the nanoamperemeter to be detected.

Figure 16 (a) shows the detector system of the setup. The detector system is mounted on an ISO-K 100 flange. The Faraday cup assembly is suspended at a tripod and consists of a cylindrical tube with a flat bottom (cup) and two repeller electrodes. Ions can enter the Faraday cup through a hole in the *vertical* repeller electrode. Isolators (yellow) separate the electrical potentials of the electrodes and the cup from the ground potential. A channeltron is mounted below a second, *horizontal* repeller electrode which is mounted on the open lower end of the cup.

To measure ion beam currents with the cup mode of the detector system, a nanoamperemeter is connected to the cup and voltages of $-200$ V are applied at both repellers (see figure 16(b)). Secondary electrons produced from the impact of the ion beam on the cylinder are thus kept inside the cup. For positive ion beams we measure a positive current and for a negative ion beam a negative current is obtained.

In the channeltron mode the cup serves as a converter plate (see figure 16 (b)) for positive and negative ion beams. The voltage at the horizontal repeller electrode close to the channeltron cone is set to $-50$ V and a voltage of $+1500$ V is applied at the channeltron cone. The secondary electrons are thus drawn from the cylinder to the channeltron.

Figure 16 (c) shows the electrical circuitry of the channeltron for single ion counting. If a particle (secondary electron) hits the cone, electrons are kicked out from the lead glass surface. A positive voltage between 2000 V and 2500 V applied between the front and the back of the channeltron accelerates the electrons towards the back of the channeltron. By creating further electrons on impact at the lead glass walls, an electron avalanche is triggered in the curved channel inside the channeltron. The anode at the end of the channeltron collects the electron avalanche. A capacitor buffers the high voltage and is used in combination with the terminating resistor $R_0 = 50\,\Omega$ to observe the negative pulse induced by the electron avalance. The signal is discriminated for its pulse height with a Constant Fraction Discriminator (CFD).

The resistor $R_2$ creates a small voltage drop, so that the anode is about 50 V more positive than the back of the channeltron. Electrons can thus be collected

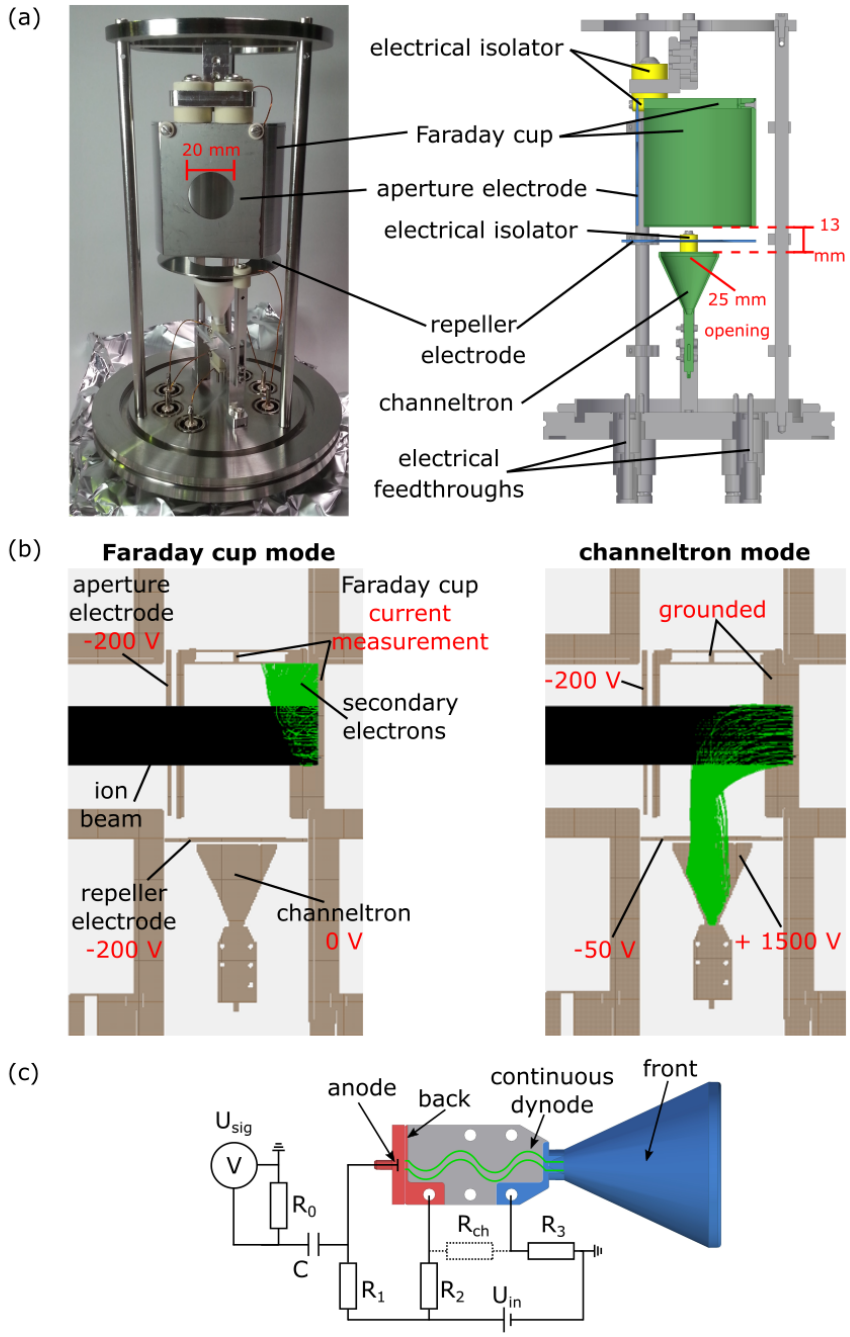


Figure 16: (a) The detector system combining a Faraday cup and a channeltron. (b) A simulation [15] of the Faraday cup mode and the channeltron mode of the detector system. (c) The electrical circuitry of the channeltron for counting. We choose $C = 1$ nF, $R_0 = 50\ \Omega$, $R_1 = 1$ M$\Omega$, $R_2 = 2$ M$\Omega$ and $R_3 = 50$ M$\Omega$. The resistance of the channeltron $R_{ch}$ is indicated with dotted lines and determined in figure 16.

efficiently. $R_1$ serves as a protective resistor. Together with the resistance $R_{ch}$ of the channeltron the resistor $R_3$ forms a voltage divider. As a result only one power supply is required.

Single samples of the negative pulse observed with an oscilloscope are presented in figure 17 (a). Different voltages $U_{ch}$ are applied between the front and the back of the channeltron. The nearby Penning vacuum gauge (giving a count rate of $\approx 10^4$ s$^{-1}$) was switched off. The samples result from dark counts with a rate of about 100 s$^{-1}$. We observe fall and rise times on the order of 4 ns. For the chosen values of $U_{ch}$ we see that those times remain constant. Figure 17 (b) shows the average pulses obtained from 128 samples for the same voltages $U_{ch}$ as in figure 17 (a). The average fall time increases with higher voltages, which may be explained by a time jitter of the oscilloscope trigger. The triggering mode is set on rising edge with a trigger level shortly below the small negative afterpulse. Additionally we observe that the average pulse amplitude increases with higher values of the voltage $U_{ch}$. The kinetic energy of the primary electrons determines the amount of secondary electrons kicked out from the lead glass walls and therefore the gain factor. The maximum gain is limited by space-charge effects.

The ohmic resistance of the channeltron typically lies in the range of 60–80 MΩ. Its precise value has to be determined individually for each device. The box containing the circuitry shown in figure 16 (c) is removed and a voltage $U_{ch}$ is applied directly between the front and the back of the channeltron. In figure 18 the measured current is plotted as a function of the voltage $U_{ch}$. The errors of the current and the voltage result from the observed fluctuation and correspond to a $1\sigma$ confidence interval. During a measurement series, the nearby Penning vacuum gauge is either off (blue data points) or on (red data points). We observe no difference between the two measurement series and an approximately linear behaviour of the measured current. We fit a line through the origin to the data points using an ODR algorithm and observe from the residuals (see figure 18 (b)) that the current is overestimated up to a voltage of 2000 V. Above 2000 V, a positive linear drift of the residuals is observed. We thus fit a line through the origin to the data points between 0 V and 2000 V (vertical dashed line) and a linear function with an offset to the data points above 2000 V. The residuals obtained with the fits show a good agreement (see figure 18 (c)). It is known that between 2000 V and 2500 V the electron gain becomes significant. The additional current observed above 2000 V may thus result from a non-ohmic behaviour of the channeltron resistance in this range. We thus consider the resistance of the channeltron measured below 2000 V as its ohmic resistance. From the series of measurements with a deactivated Penning vacuum gauge we determine $R_{ch} = 73.28(10)$ MΩ. The errors are the propagated errors of the fit. The reduced chi-squared value is $\chi_{red} \approx 0.61$.

The measured ohmic resistance $R_{ch}$ of the channeltron, the resistors $R_2 = 2$ MΩ and $R_3 = 50$ MΩ form a voltage divider. If we apply the input voltage $U_{in}$, the

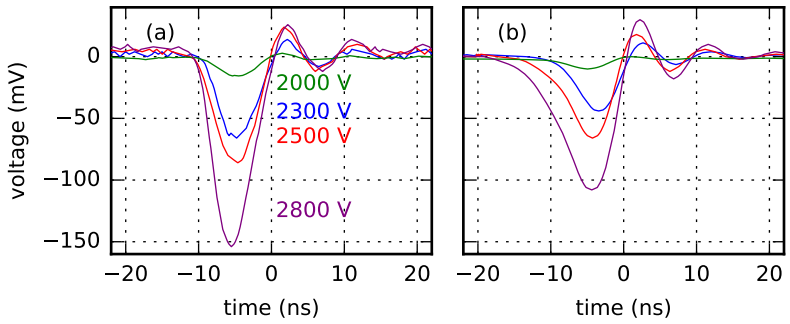


Figure 17: The signals induced by a single particle at the channeltron are presented for different voltages $U_{ch}$ applied between the front and the back of the channeltron. In (a) a single samples are plotted and in (b) the average of 128 pulse samples is given for each voltage.

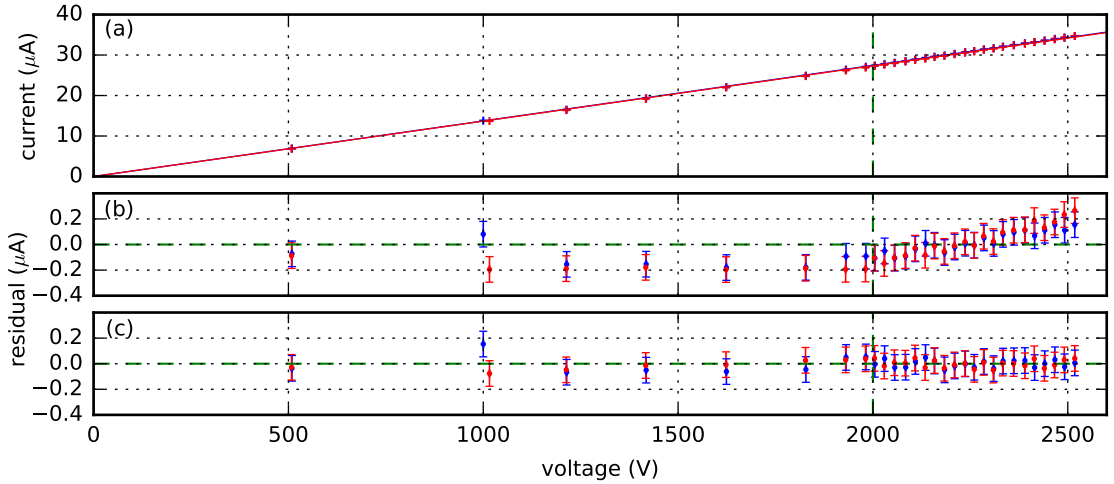


Figure 18: (a) The measured current as a function of the voltage applied between the front and back of the channeltron is presented. The measurement series is performed with a nearby Penning vacuum gauge switched off (blue) and switched on (red). (b) The residuals of the fit of a line through the origin to all data points are shown. (c) The residuals of two linear fits are given. The first set of data points from 0 V–2000 V is fitted with a line through the origin. The data points above 2000 V are fitted with a linear function with an offset.

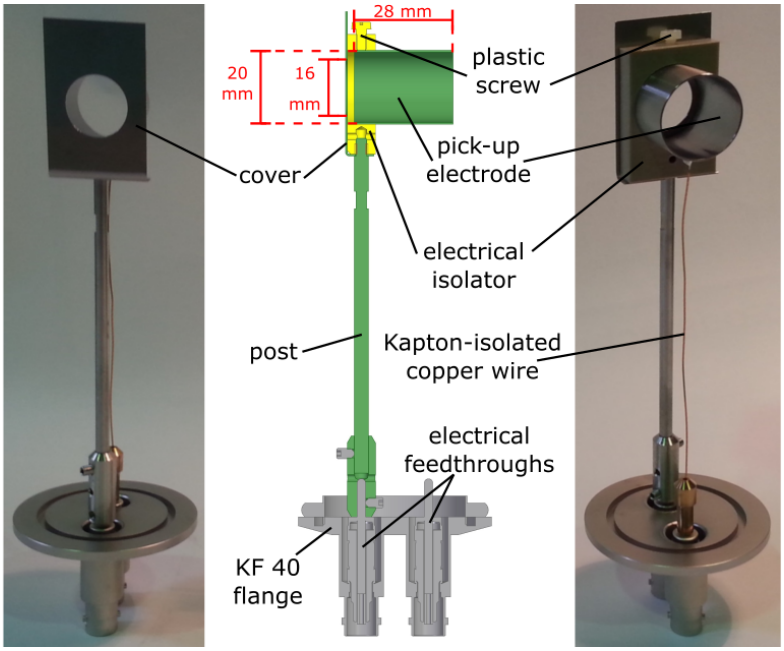


Figure 19: A pick-up electrode for detecting pulsed ion beams is presented.

voltage

$$U_{ch} = U_{in} \frac{R_{ch}}{R_2 + R_{ch} + R_3} \tag{13}$$

drops between the front and the back of the channeltron, which corresponds to 58.49(3)% of the input voltage. Correspondingly, a voltage of

$$U_{front} = U_{in} \frac{R_3}{R_2 + R_{ch} + R_3} \tag{14}$$

and therefore 39.91(3)% of the input voltage is applied at the cone of the channeltron.

## 3.2 Pick-up electrode

Pulsed ion beams are detected non-destructively with a pick-up electrode. When an ion bunch enters and leaves a pick-up electrode, a change in the induced image charge is observed. It may be used for time-of-flight applications. From the integrated signal the total charge in the ion bunch can be inferred.

Figure 19 shows the detector which is built in before and after the magnet of the setup (see figure 5 (b) and (c)). The post of the detector is mounted onto the pin of a BNC feedtrough. The pick-up electrode is electrically isolated from the post by a PEEK isolator. A cover electrode with an opening of 16 mm protects this

isolator from electrostatic charge caused by the ion beam. The cover electrode is electrically connected to the post and both cover and post are usually grounded during operation. The signal of the pick-up electrode is transported to a second BNC feedtrough with a Kapton-isolated wire running in the shadow of the post to screen it from ion impact.

The assembly is mounted on a single ISO-KF 40 flange. The axis of the post is not coincident with the rotation axis of the flange, which affects the alignment procedure. Thus the pick-up electrode axis is aligned relative to the flange before the electrode can be mounted to the chamber and aligned with the telescope. The inner alignment is repeated until the pick-up electrode is also well aligned with the beam axis viewed by the telescope. For the mass spectrometer this design is considered to be a good trade-off between compactness and alignment effort.

After the pick-up electrodes were built in, their capacitance was measured relative to the surrounding vacuum chamber. We determined the capacitance directly at the electrical feedthrough and performed the measurement for floating cover and post (see figure 19) as well as when the cover and post were connected to the grounded vacuum chamber. The measured capacitance is presented in table 1. The errors result from the observed fluctuation.

The image current induced by an ion bunch entering and leaving the pick-up electrode can be observed directly with a fast current amplifier. The observed signal is presented in section 4.3.

Table 1: The measured capacitance $C_1$ and $C_2$ of the pick-up electrode before and after the magnet for floating and grounded covers/posts (see figure 19) is presented. The errors correspond to a $1\sigma$ confidence interval.

| state of cover and post | $C_1$ (pF) | $C_2$ (pF) |
|---|---|---|
| floating | 12.0(1) | 11.9(1) |
| grounded | 13.1(1) | 12.9(1) |

# 4 Characterizing the setup with a Penning ion source

## 4.1 Mass spectrometry

### 4.1.1 Mass spectra for different carrier gases and beam energies

The setup is characterized with a Penning ion source using argon and nitrogen as carrier gases. The positive ions inside the Penning ion source are accelerated to a kinetic energy up to 12.5 keV or 5 keV for argon and 12.5 keV for nitrogen. The resulting beams and their composition are analyzed by varying the magnetic field and measuring the ion current at the Faraday cup after the magnet. For each beam energy and carrier gas, the magnetic field is calibrated with the corresponding masses of two clearly identifiable peaks. The detailed calibration procedure is described in section 4.1.2. Mass spectra for the three different ion beams are presented in figure 20. For the following analysis, we define a peak as an amplitude of the cup signal with an intensity $I > 5\sigma_n$, where $\sigma_n$ is the standard deviation of the signal noise.

Below a mass of 12 u and above a mass of 46 u, no peaks were found. The plotted mass spectra are thus limited to this interval. To obtain the mass spectra in this range, the magnetic field was scanned between 112 mT and 220 mT for the 5 keV ion beam and between 177 mT and 347 mT for a beam energy of 12.5 keV.

At a beam energy of 5 keV the ion current measured at the Faraday cup is about an order of magnitude lower than at 12.5 keV. For each carrier gas, only one peak with a high intensity is found. The peak next in intensity is about 10 times weaker and observed to be at half of the mass of the strongest peak. The rest of the peaks is weaker by a factor of 5 to 230. Pronounced tails can be observed for most of the peaks in the spectra taken for the 5 keV beam (see figure 20 (e)). For the 12.5 keV beams, the tails are strongly suppressed (see figure 20 (c) and (h)). Peaks with a similar intensity have a Full Width at Half Maximum (FWHM) on the same order of magnitude. The peak width may result from the energy uncertainty of the ions created in the gas discharge and the spatial manipulation by the slits before the magnet. The observed tails may be explained by collisions of ions with the slits and apertures before the magnet due to a higher beam divergence at lower beam energies.

In the spectra given in figure 20, the intensity is plotted against the mass-to-charge ratio which is converted to a reduced mass assuming ions carrying only a single charge $q = e$. The peak observed at the reduced mass 13.33 u/$e$ can not be explained with a singly charged particle. Reasonably this mass-to-charge ratio results from a triply charged state which corresponds to the mass of the most abundant argon isotope $^{40}$Ar. Since the Penning ion source is known [38] to produce higher charge states of the carrier gases and the triply charged state of argon is observed, the strong peak at the reduced mass 20 u/$e$ is explained by $^{40}Ar^{2+}$.

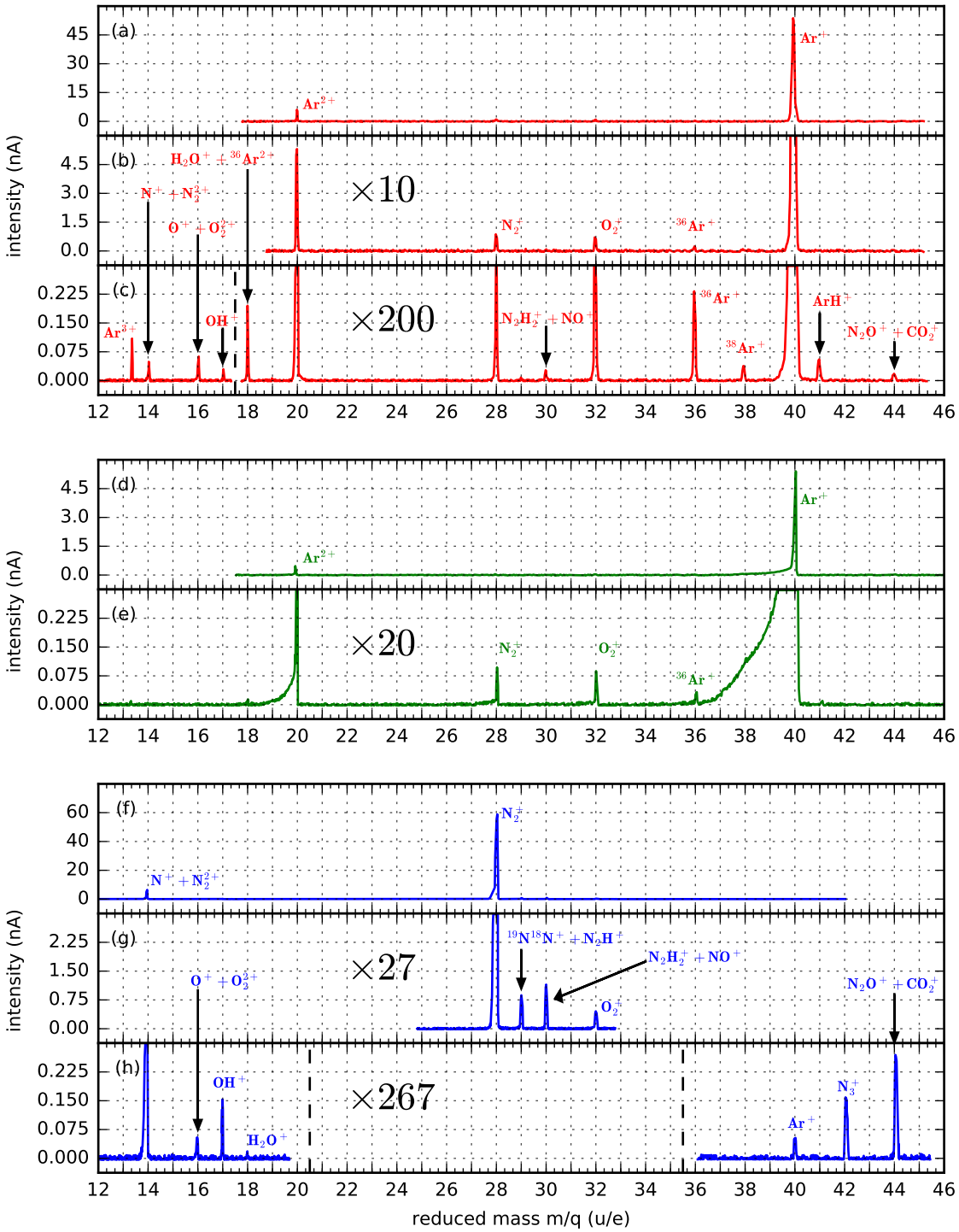


Figure 20: The mass spectra of the 12.5 keV (red) and 5 keV (green) ion beams produced by the Penning ion source with argon gas, and the 12.5 keV beam (blue) produced with nitrogen gas are presented. The reduced mass was determined from the magnetic field for singly charged ions. Panel (c) and (h) each show two spectra separated by vertical dashed lines.

In a similar way the peaks found in the spectra taken with nitrogen carrier gas (see figure 20 (f)–(h)) at the reduced masses 28 u/$e$ and 14 u/$e$ are explained by $^{14}N_2^+$ and $^{14}N_2^{2+} + {}^{14}N^+$, which can not be resolved.

Many weaker peaks occur in the spectra in figure 20 at reduced masses where one would expect to find ions resulting from the most abundant gaseous components of air—such as $N_2$, $O_2$, Ar, $CO_2$ and $H_2O$ [6]—and their reaction products. Such ions may be produced by air which diffuses into the Teflon tube transporting the carrier gas from the gas bottle to the gas inlet (see figure 9) or by internal or external gas leaks at the O-ring sealed surfaces of the source. Similar to the carrier gas, the air could then undergo ionization and chemical reactions in the gas discharge. Although the setup was pumped for about two days after a carrier gas exchange a small fraction of argon was still left when a beam was produced with nitrogen gas (see figure 20 (h)).

The relative intensities of the peaks at reduced masses 36, 38 and 40 were examined. For the 12.5 keV beam produced with argon gas, the reduced mass 20 and reduced mass 36 peaks were used to normalize the intensities of the peaks at reduced mass 36 and 38 to the intensity of the strongest peak at reduced mass 40. The measured peak ratios are in good agreement with the natural abundances (see table 2) considering a $2\sigma$ error. The error results from the fluctuation of the signal at the Faraday cup. It was estimated to be 4.7% by observing the cup signal at the reduced mass 40 peak over the time range of 15 min, which is approximately the time needed to perform a magnetic field scan. Thus we infer that the peaks at reduced masses 36, 38 and 40 result from the isotopes of the carrier gas argon.

The natural abundance of $^{14}N$ also agrees well with the value obtained from the spectrum measured with nitrogen carrier gas. It was derived from the absolute intensities of the peaks at reduced mass 28, 29 and 30. Even though the measured natural abundance of $^{15}N$ disagrees with the literature value (see table 2), the peak

Table 2: The measured isotopic abundances of argon and nitrogen are presented. The reference values are given as stated in [21]. The given errors correspond to a $1\sigma$ confidence interval.

| atomic number $Z$ | element symbol | mass number $A$ | measured relative abundance | reference value |
|---|---|---|---|---|
| 18 | Ar | 36 | 0.004 2(6) | 0.003 336(210) |
| | | 38 | 0.000 80(11) | 0.000 629(70) |
| | | 40 | 0.995 0(7) | 0.996 035(250) |
| 7 | N | 14 | 0.986 2(2) | [0.995 78, 0.996 63] |
| | | 15 | 0.110 04(9) | [0.003 37, 0.004 22] |

at reduced mass 28 can be assumed to result from the most abundant isotope in the nitrogen carrier gas.

The intensity ratio $k_{21} = I_2/I_1$ was determined from the intensities $I_2$ and $I_1$ of the peaks resulting from the doubly and singly charged state of $^{40}$Ar. It was observed to be $k_{21} = 0.092(12)$ at a beam energy of 12.5 keV. Isotopes with the same atomic number $Z$ have very similar chemical properties due to their similar electronic structures [8] and therefore a similar ionization potential. Thus the doubly charged state of $^{36}$Ar and its singly charged state should have a similar ratio compared to $^{40}$Ar (see figure 20 (c)). The observed ratio $k''_{21} = 0.84(4)$ for $^{36}$Ar strongly disagrees with the expected value $k_{21}$. Thus, the peak at reduced mass 18 is assumed to be dominated by $H_2O^+$.

### 4.1.2 Calibrating the mass spectrometer

To obtain the presented mass spectra with the experimental setup, the magnetic field $B$ was calibrated with literature mass values [21] of species that could be clearly identified in the magnetic field spectra. In the following, we will discuss the calibration procedure for the beam produced with argon gas at an energy of 12.5 keV. A diagram of the procedure is shown in figure 21. The spectra obtained for argon gas at 5 keV and nitrogen gas at 12.5 keV were calibrated in a similar fashion.

The positive ion beam current $I_F$ at the Faraday cup is measured as a function of the magnetic field $B$ of the bending magnet. The constant positive offset resulting from the ampere meter itself is corrected. When the power supply of the magnet is off, a small time-dependent negative offset of the magnetic field on the order of $-2$ mT is observed (see figure 22). It draws near zero when the hall probe is removed from between the pole shoes. The offset can be explained with local remanence. Due to the construction of the magnet (see figure 12) the magnetic field has to be measured at a horizontal distance of $d_H \approx 5$ cm from the estimated ion trajectory. The magnetic field offset is measured before each series of measurements and corrected.

The obtained corrected spectrum (see figure 21 (a)) shows two peaks with an intensity >5 nA at the magnetic flux densities $B \approx 227$ mT and $B' \approx 322$ mT. The absolute uncertainty of the peak positions is estimated to be 50% of the FWHM corresponding to a relative uncertainty of $\approx 0.1\%$. We know [38] that a Penning ion source also produces higher charge states of the carrier gas. We thus identify the peaks with the highest and second highest intensity as $^{40}Ar^+$ and $^{40}Ar^{2+}$ and assign the values $B$ and $B'$ to the mass-to-charge ratios $m/q = 20$ u$/e$ and $m'/q = 40$ u$/e$.

Then the two data points are fitted with the function

$$\frac{m}{q} = \frac{(Br)^2}{2U} \tag{15}$$

From the covariance matrix we find that the parameters $U$ and $r$ are strongly correlated. The parameter $r$ is expected to be about $r = 0.300(9)$ m due to a geometrical examination of the pole shoe.

Because of the choice of the electrical circuitry (see figure 8), the extraction voltage $U_{ex}$ determines the upper limit of the voltage $U$ at which ions inside the Penning ion source are created. The anode voltage $U_{an} > 0$ thus defines the lower limit $U_{ex} - U_{an}$. If both $U$ and $r$ are left free during the fit, parameters far beyond the expected values are obtained. This motivates the search for a different ansatz.

We find that the residuals do not change significantly when one parameter is scanned in order to determine the other parameter from the fit. The behavior is independent of whether $U$ or $r$ is the varied parameter. The parameter $U$ is scanned in the interval $[U_{ex} - U_{an}, U_{ex}]$ and the resulting radius is plotted as a function of the voltage $U' = U - U_{ex}$. The same is done for the 5 keV beam produced with argon gas. The measured extraction voltage for both the 5 keV and the 12.5 keV beams are given in table 3.

The resulting curves are plotted in figure 21 (c). A band of the possible effective radii $r$ and voltages $U'$ is obtained for each beam energy and carrier gas. The curves obtained for argon at 5 keV and 12.5 keV form an intersecting plane. All of the mass spectra shown in figure 20 were obtained for identical settings of the apertures and slits (see figures 5 (b) and (c)) manipulating the beam spatially and defining the bending radius $r_b$ of the magnet. The anode voltage $U_{an}$ was also left unchanged. As a consequence the ions created in the gas discharge see the same ambient potential regardless of the choice of the extraction voltage $U_{ex}$. The voltages of all electrostatic ion-optical elements were scaled down in accordance

Table 3: The measured extraction voltage $U_{ex}$ and the fit parameters $U$ and $r$ obtained from the calibration procedure are presented for different beam energies and carrier gases. The given errors are statistical errors resulting from the calibration procedure and correspond to a $1\sigma$ confidence interval. For completeness, the applied anode voltage $U_{an}$ is given.

| carrier gas | beam energy (keV) | $U_{an}$ (V) | $U_{ex}$ (kV) | $U$ (kV) | $r$ (m) |
|---|---|---|---|---|---|
| Ar | 5 | | 5.0742(13) | 4.971(12) | |
| | 12.5 | 789.2(6) | 12.48(3) | 12.38(3) | 0.3148(2) |
| $N_2$ | | 900(40) | 12.48(3) | 12.27(3) | |

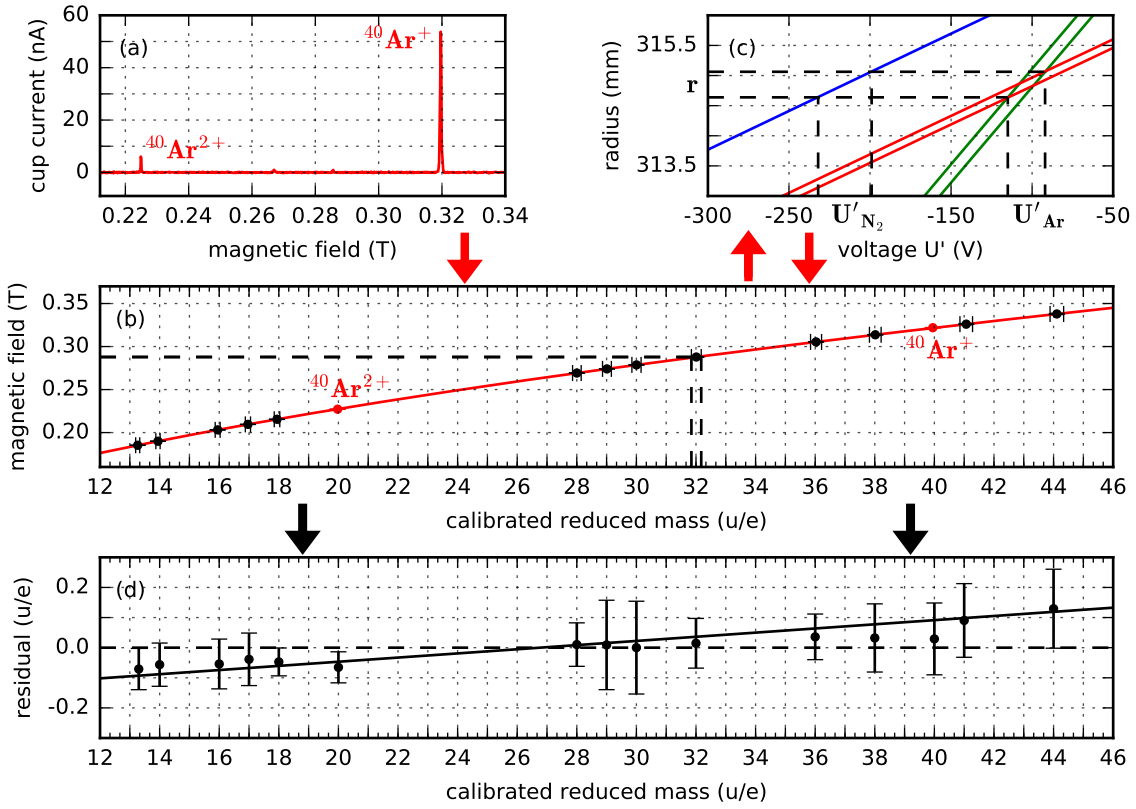


Figure 21: The calibration procedure of the mass spectrometer is presented for the 12.5 keV beam produced with argon gas. Red and black arrows indicate the data flow. (a) The cup current $I_F$ is measured as a function of the magnetic field $B$. The values of $B$ at two peaks with the highest intensity ($^{40}Ar^{+}$ and $^{40}Ar^{2+}$) and the corresponding reduced masses m/q for a singly charged ion are determined in u/e. (b) The magnetic field is calibrated with these data points by a fit (red curve). A peak found at a magnetic field $B$ can thus directly be converted to a reduced mass $m_c$. (c) The fit of the two data points was repeated for given values of the parameter $U$. The radius parameter $r$ resulting from the fit was plotted as a function of the voltage $U' = U - U_{ex}$ with the maximum extraction voltage $U_{ex}$ (red lines). The same was done for the 5 keV beam produced with argon gas (green lines). The radius $r$ and the parameter $U_{\mathrm{Ar}} = U'_{\mathrm{Ar}} + U_{ex}$ were estimated (black dashed lines) from the intersecting area and used as final parameters for the fit in (b). Based on the value obtained for $r$ the parameter $U_{\mathrm{N_2}} = U'_{\mathrm{N_2}} + U_{ex}$ of the beam produced with nitrogen was determined (blue line). (d) Reduced masses $m_c$ derived with the calibration curve in (b) were assigned to the nearest integer reduced masses $m_a$. The residuals $m_c - m_a$ were plotted versus the calibrated reduced mass $m_c$. The errors correspond to a $1\sigma$ confidence interval.

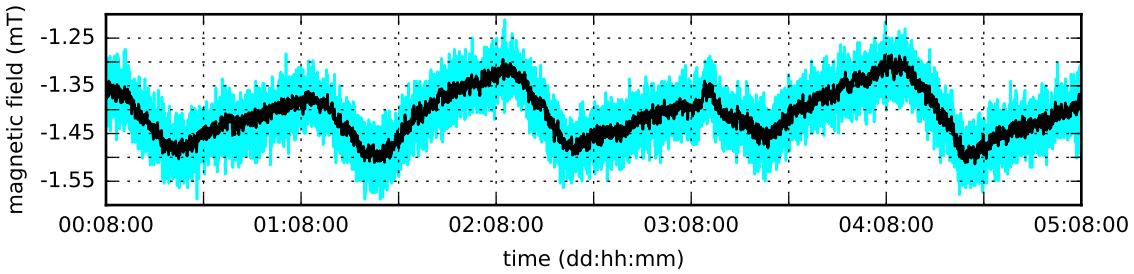


Figure 22: The magnetic field measured with the Hall sensor between the pole shoes is observed for a switched off magnet over five days. The original data curve (cyan) is smoothed by averaging over 10 neighboring data points (black curve). This corresponds to a time interval of 300 s. The signal varies periodically with a cycle duration of $T \approx 24$ h and has a variable amplitude.

with the extraction voltage. With this knowledge we assume that the fit parameter $r$ has to be identical for the two energies of the beams produced with argon. Its uncertainty is defined by the boundaries of the intersecting plane. The parameter $U = U_{ex} + U'$ can then be inferred for argon at 5 keV and 12.5 keV (see figure 20 (c)). For nitrogen carrier gas, the parameter $U$ was inferred with the radius parameter $r$ determined for argon. The effective radius $r = 0.3148(2)$ and the values for the parameter $U$ given in table 3 are obtained with a relative precision on the order of 0.2 % considering $1\sigma$ errors. We observe that the effective radius agrees with the bending radius $r_b = 300(9)$ estimated from a geometrical examination of the pole shoes considering $2\sigma$ errors. This is not surprising since the precise contribution and coverage of the fringing fields at the edges of the pole shoes are not known. They can only be estimated from a detailed simulation of the magnetic field. For the further analysis, the values obtained for $r$ and $U$ are assumed for the bending radius of the magnet and the effective potential at which the ions are born inside the source (see equation (5) in section 2.1).

The calibrated reduced masses $m_c$ for the identified peaks are assigned to the

Table 4: The slope $\alpha$, the offset values $\beta_i$ and the reduced chi-squared obtained for a simultaneous fit of the residuals are presented. The given errors result from the fit and correspond to a $1\sigma$ confidence interval.

| carrier gas | beam energy (keV) | $\alpha$ | $\beta_i$(u/e) | $\chi^2_{red}$ |
|---|---|---|---|---|
| Ar | 5 | 0.0069(18) | -0.20(6) | 0.10 |
| | 12.5 | | -0.18(5) | |
| $N_2$ | | | -0.08(5) | |

nearest integer reduced mass $m_a$ and the residual $m_c - m_a$ is plotted against the calibrated reduced mass $m_c$ (see figure 21 (d)). A good agreement considering $2\sigma$ errors is observed except for the peak at reduced mass 13. Assigning the peak to a reduced mass $m/q = 40$ u$/3e \approx 13.33$ u$/e$ resulted in a good agreement considering $2\sigma$ errors.

In figure 21 (d) one can see the that for low reduced masses the assigned reduced mass is slightly underestimated. With increasing reduced mass the deviation turns into a slight overestimation in a linear fashion. The residual plots obtained for argon at 5 keV and nitrogen at 12.5 keV have a very similar drift behavior but a different offset. The three residual plots were thus fitted simultaneously with linear functions

$$m_r = \alpha m_c + \beta_i \tag{16}$$

with the global slope $\alpha$ and the axial intercepts $\beta_i$ different for each of the three plots. The obtained fit parameters and the reduced chi-squared value $\chi^2_{red}$ of the simultaneous fit are given in table 4.

According to (5) a linear drift in the reduced mass residual (see figure 21 (d)) corresponds to a quadratic drift of the magnetic field. From the observed mass drift it is estimated to be on the order of $\approx 1$ mT over the observed mass range. The magnetic field was measured at a horizontal distance of about $d_H \approx 5$ cm away from the estimated particle trajectory and closer to the edge of the pole shoe. The drift can be explained by magnetic fringing fields and inhomogeneities.

Figure 13 shows the hysteresis curve measured for the magnet with the Hall sensor at the same position as for the spectrum measurements. We do not know the detailed properties of the magnetic field between the pole shoes. The key component of the dipole magnet are the two live coils creating the magnetic field. In the center between the two coils the field has the highest homogeneity and magnetic flux density $B$. The further we go away from the center, the higher the effect of field inhomogeneities and the lower the magnetic flux density $B$ becomes. We assume that the magnetic field at the ion beam trajectory between the pole shoes is higher than at the measurement point. Saturation effects thus occur earlier for the same coil current $I_{coil}$. For low currents the magnetic field is thus underestimated. The magnetic field necessary to deflect an ion with reduced mass $m$ towards the Faraday cup is thus higher than measured. As a consequence the measured $B$ field value is assigned with an overestimated calibrated reduced mass $m_c$. Due to the assignment to the nearest integer reduced mass $m_a$ the residual $m_c - m_a$ is thus negative. With advancing saturation effects we expect that the underestimation of the magnetic field becomes smaller, resulting in a positive drift of the residual.

The difference in the offsets $\beta_i$ of the fits is explained by the fact that the two peaks used for the calibration were taken in different magnetic field intervals due to the different carrier gases and beam energies.

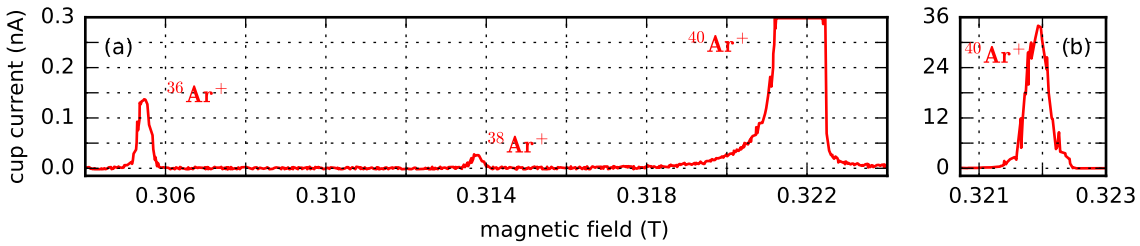


Figure 23: The optimized peak shape for the 12.5 keV beam produced with argon is presented. Both the cup current offset and the teslameter offset were corrected.

For each carrier gas and beam energy the drift-corrected masses

$$m_d = m_c - m_r \tag{17}$$
$$= m_c - \alpha m_c - \beta_i \tag{18}$$

are determined by subtracting the fitted linear function (16) from the reduced masses $m_c$ determined from the calibrated parameters $U$ and $r$ (see table 4). With this procedure, the mass spectra shown in figure 20 are obtained from the magnetic field spectra as functions of measured quantities.

### 4.1.3 Peak shape and resolving power

Before spectra can be taken, the peak shape has to be optimized. The optimized magnetic field spectrum is shown in figure 23 for the 12.5 keV ion beam produced with argon gas. The cup current is plotted as a function of the magnetic field $B$. An approximately symmetrical peak shape can be observed.

We determine the resolving powers $R = m/\Delta m$ [2] from the position and the FWHM of the $^{36}Ar^+$ peak and the $^{40}Ar^+$ peak and find $R_{^{36}Ar^+} = 407(4)$ and $R_{^{40}Ar^+} = 415(4)$. The errors mainly result from the errors of the parameters $U$ and $r$ (see table 3) used to convert the magnetic field to mass values. For a 12.5 keV beam produced with a Penning ion source the mass spectrometer can thus separate the masses 400 and 401 from each other.

For fully opened slits before and after the magnet a peak structure consisting of a high center peak and two lower side peaks was observed for all of the peaks of the spectrum. This unwanted structure could be removed by setting the horizontal and vertical slit pairs before and after the magnet to a 2 mm by 2 mm opening each and by building in the 1 mm aperture shown in figure 5 (c). All of the spectra shown in this work were obtained for this configuration.

It was found that the anode voltage $U_{an}$ of the Penning ion source has the highest impact on the peak width. It has to be chosen as low as possible. The lowest value

with a stable beam output was found to be $U_{an} \approx 700$ V. The first einzel lens belongs to the Penning ion source. It was set to a voltage of $U_{el1} \approx 9.5$ kV. The optimal voltage of the second einzel lens belonging to the setup was found to be $U_{el2} \approx 5.8$ kV at $U_{ex} = 12.5$ keV. It was observed that the einzel lens of the Penning ion source ($U_{el1}$) is more important for the peak intensity. If it is switched off and the second einzel lens is still on, the beam intensity measured at the cup is reduced by a factor of 20. For the first einzel lens switched on and the second einzel lens switched off the cup signal reduces only by a factor of 3.

After the pick-up electrodes were added to the setup, a continuous negative current on the order of $-2$ nA was measured at the pick-up electrode (see figure 19) in front of the magnet while a beam was produced. At the same time, tail-like structures smearing out the peaks to lower values of the $B$ field were observed in the spectra. When a negative voltage of $U_{cover} \approx -30$ V was applied at the cover directly before the pick-up electrode, a positive current on the order of 10 nA was measured at the pick-up electrode. We thus infer that the current seen at the pick-up is a net current resulting from electrons produced at the slits directly before the pick-up electrode and a fraction of the positive ion beam hitting the pick-up electrode. The tail-like structures could be removed from the spectrum by steering the beam in order to minimize the absolute value of the current observed at the pick-up electrode. For optimized settings, voltages between $U_{steerer} \approx -410$ V and $U'_{steerer} \approx 50$ V were applied between the plates of the steerer pairs.

## 4.2 Counting ions in a pulse

As discussed in section 3.1, the Faraday cup of the detector system at the end of the beamline (see figure 5 (c)) serves as a converter plate when the channeltron is active (see figure 16 (b)). It was seen that a current of 1.6 pA is the estimated limit ($10^7$ s$^{-1}$) for ion counting. However, for ion currents on the order of 200 pA it is observed that changing the voltage of the horizontal repeller (see figure 16 (a)) to $-400$ V leads to a rate at the channeltron in the countable range. For the given settings of the suppressed counting mode (see table 5), the count rate was suppressed by a factor of about $10^3$. This behavior was further examined with a Penning ion source using argon as carrier gas and an extraction voltage of 12.5 kV.

The ion beam is extracted from the source and chopped at the vertical slits before the magnet by switching the applied voltages at the second vertical steerer pair (see figure 5 (b)) between 0 V and 2 kV. The resulting bunches arrive at the detector system after the magnet. There the ions hit Faraday cup serving as a converter plate and electrons are emitted. A fraction of these electrons is accelerated to the channeltron and counted. The beam intensity is varied by defocusing the beam with the second einzel lens and the count rate at the channeltron is measured as a function of the cup current which is determined before and after each counting step

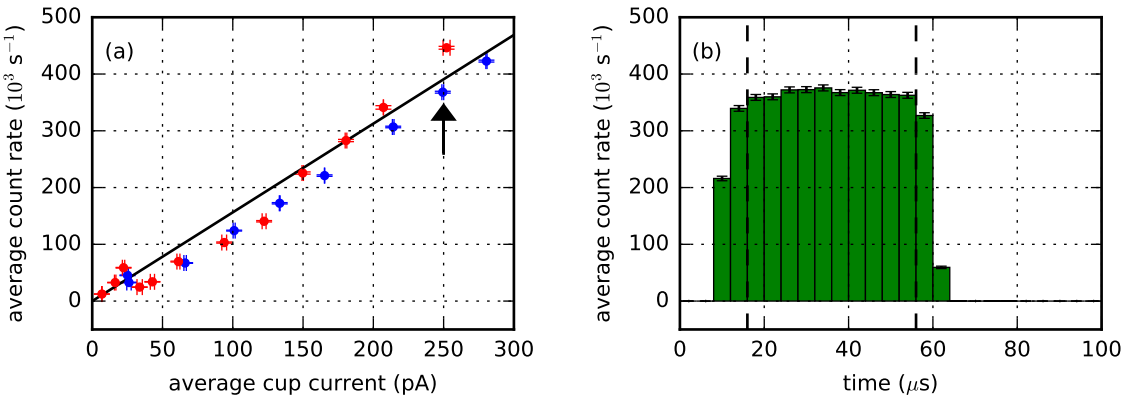


Figure 24: (a) The average rate of $^{40}Ar^{2+}$ ions counted in the pulses of a chopped ion beam is plotted as a function of the mean cup current determined before and after each counting measurement. The results of two measurement series performed with bunch durations of 50 µs (blue data points) and 70 µs (red data points) are presented and a line through the origin is fitted to the data points. (b) The average time structure of the 50 µs pulses obtained for a cup current of $I \approx 250$ pA (black arrow in (a)) is presented. The count rate is plotted against the time elapsed relative to the point of time of the trigger signal. Black dashed lines indicate the interval used to determine the average count rate in (a).

by disabling the chopping. The goal is to find out whether the obtained relation between the signals could be used for calibrating the channeltron with the cup.

In figure 24 the results obtained for $^{40}Ar^{2+}$ ions and bunch durations of 50 µs (blue) and 70 µs (red) are presented. Figure 24 (a) shows the average count rate plotted against the average cup current for the suppressed counting mode. For each measurement the beam was chopped with a rate of 10 Hz and at least 6000 counts were accumulated. The error bars, representing the $1\sigma$ confidence interval, result from the statistical error of the count rate and the mean error of the cup current measured before and after each counting step. We observe a roughly linear behavior of the count rate with increasing cup current. For both measurement series the voltage settings of the detector system (see table 5) were the same. A line through the origin is thus fitted to the data points using an ODR algorithm yielding a slope $a = 1560(40)\text{s}^{-1}\text{pA}^{-1}$ and a reduced chi-squared value $\chi^2_{red} \approx 1638$.

Figure 24 (b) shows the average time structure obtained for a 50 µs bunch at a cup current of 250 pA (black arrow in figure 24 (a)). The average count rate is plotted as a function of the time elapsed since the chopping trigger pulse. The shown errorbars result from the statistical error of the count rate. We observe a rise and fall time of about 8 µs and and a plateau with an approximately constant

count rate of $3.8 \times 10^5$ s$^{-1}$. Considering the rise and fall times the bunch duration is found to be 48(6) µs. For the average count rate given in figure 24 (a) only the plateau was used (black dashed lines). The average count rate of the 70 µs bunches (blue data points) was obtained in the same fashion.

One measurement step is performed in a time range on the order of 15 min. In section 4.1 the beam intensity was estimated to fluctuate about 4.7% over this time interval. We thus exclude that the deviation of the data points from the fit results from a fluctuation of the beam intensity during the counting measurements. It may be explained by counting background electrons which are created at the slits before the detector or at the vertical repeller and enter the channeltron via the small gap between the repeller electrode and the channeltron cone (see figure 16 (a)). The defocusing with the einzel lens changes the beam properties and may thus have an influence on the amount of background electrons created. Furthermore changes in the spatial distribution of the electrons may also induce nonlinear effects between the cup and the channeltron mode.

## 4.3 The pick-up signal of an ion pulse

The pick-up electrode after the magnet was tested with 5 µs bunches of $^{40}Ar^+$ ions with a kinetic energy of 12.5 keV created at a rate of 10 Hz in the same fashion as described in section 4.2. The pick-up signal and the cup signal of an ion bunch were measured with fast current amplifiers with a sensitivity of $1 \times 10^{-7}$ A/V and a bandwidth of 400 kHz corresponding to a rise time of 900 ns. The average signals of 128 samples and the trigger signal for chopping the beam are presented in figure 25. The pick-up electrode before the magnet was not tested due to a high negative signal background resulting from electrons created at the slits.

The signal at the pick-up electrode (red) and at the Faraday cup (green) are plotted as a function of the time elapsed since the trigger signal (blue curve and axis). In the time window of the trigger pulse we observe a small negative signal at the pick-up electrode. Considering the time-of-flight $t_{tof} \approx 11$ µs of the $^{40}Ar^+$ ions for a distance of 2.5 m, we can exclude that this pick-up signal results from the ion

Table 5: The voltage settings of the vertical repeller $U_{rep,v}$, the horizontal repeller $U_{rep,h}$ and the channeltron $U_{in}$ (see figure 16 (c)) used during all measurement series (see figure 24) are presented.

| measurement mode | $U_{rep,v}$ (V) | $U_{rep,h}$ (V) | $U_{in}$ (V) |
|---|---|---|---|
| normal counting | −200 | −50 | +4106 |
| suppressed counting | −200 | −400 | +4106 |
| Faraday cup | −200 | −200 | 0 |

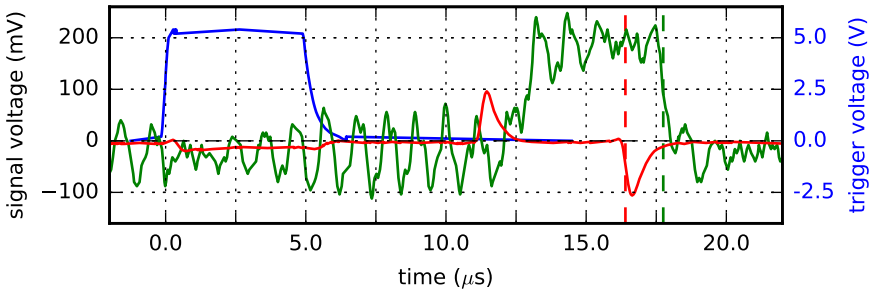


Figure 25: The average signal of 128 samples of a 5 µs bunch of $^{40}Ar^{+}$ ions measured with fast current amplifiers at the pick-up electrode after the magnet (red) and the Faraday cup (green) is presented as a function of the time elapsed since the chopping trigger pulse (blue signal and axis).

bunch. It was found that the signal is due to noise from the fast switching of the chopping voltage.

We see a positive peak (red) when the bunch of positive ions enters the pick-up electrode and a negative peak when it leaves the pick-up electrode. In between, the induced image charge does not change and no signal is observed for about 5 µs. The first peak has a rise time of 224 ns, a fall time of 740 ns and a FWHM of 510 ns. For the second peak we observe a fall time of 240 ns, a rise time of 1020 ns and a FWHM of 590 ns. The rise and fall times are lower than the time resolution given by the fast current amplifier. Compared to the cup signal (green), we observe a low noise on the pick-up signal.

The cup signal (green) is shifted by the flight time of the ions between the pick-up electrode and the Faraday cup. It has an amplitude of 200 mV corresponding to a current of 20 nA. Thus a 5 µs bunch consists of about $6.2 \times 10^5$ singly charged ions. Despite averaging over 128 samples a strong oscillating background in the cup signal is observed. We find that it results from the power supplies of the horizontal or vertical repeller electrode.

# 5 Conclusion and outlook

In the course of this work a mass spectrometer with a 60° bending magnet was set up and characterized with a Penning ion source. Mass spectra of ion beams produced from argon carrier gas at energies of 5 keV and 12.5 keV or nitrogen carrier gas at 12.5 keV were taken. The pick-up electrode after the magnet and the detector system comprising a Faraday cup and a channeltron were tested with a 12.5 keV beam produced from argon gas as well as $N_2$.

For argon, all peaks in the mass spectra obtained in the range between 12 u and 46 u could be explained with species resulting from the carrier gas or from components of the ambient air entering the Penning ion source due to internal or external leaks. The resolving power $R \approx 400$ of the mass spectrometer was determined from the spectra. We obtained that the 60° magnet can deflect ions up to a mass-to-charge ratio of 1200 u/$e$.

By using the relation $B(m) = C\sqrt{m}$ with $C = \sqrt{2U/(qr^2)}$, the mass spectra were calibrated without the prior knowledge of the precise bending radius $r = r_b$ and the electric potential $U$ at which the ion beam is created. Instead, the possible parameter space formed by $r$ and $U$ was estimated for two different extraction voltages and otherwise identical settings of the setup. The overlap of the parameter spaces yielded $U$ and $r = 0.3148(2)$ m with a relative precision of 0.2% or better. In principle, this method can be used for any setup where the two parameters are not known precisely. A further examination of this method for additional extraction voltages is needed.

After the calibration process a residual peak shift from $B(m)$ was observed over the range of the mass spectrum. This effect was explained with saturation effects of the magnetic field progressing faster in the center between the pole shoes than close to their edges, where the magnetic field is measured. For the further analysis the drift was corrected. The pole shoes thus have to be modified so that the magnetic field can be measured directly below the ion trajectory.

For ion beams with an intensity on the order of 200 pA it was observed that the rate measured at the channeltron can be controlled by the voltage applied at the horizontal repeller electrode before the channeltron cone. A reduction by a factor of $10^3$ can be obtained, leading to about $3 \times 10^5$ s$^{-1}$ instead of the full-efficiency rate of $3 \times 10^8$ s$^{-1}$. A roughly linear relation between the current measured at the Faraday cup and the count rate of the channeltron was found. Possible systematic effects are considered to result from background electrons and a variation of the spatial distribution of the beam hitting the converter plate. For suppressing stray electrons it is recommended to encase the entire detector system as well as possible. It may also be better to use an ion source that can be regulated in intensity without affecting the spatial properties of the ion beam.

We tested the pick-up electrode after the magnet with fast current amplifiers and bunches of $^{40}Ar^{+}$ ions and observed that the induced peaks in the signal had a FWHM between 510 ns and 590 ns. Two pick-up electrodes may thus be used for time-of-flight mass spectrometry with heavy cluster systems produced by an LVAP. We suggest to use a magnet with a straight port for this purpose.

In summary, we find that the experimental setup is suited to examine the pulsed beams of an LVAP and continuous ion beams produced by a Penning ion source or a MISS. Its detector systems can detect both weak and strong beams and the obtained results pose a first step to closing the sensitivity gap between a counting detector and a nanoamperemeter. Additional modifications for the mass spectrometry of heavy cluster systems are required.

## List of Figures

## List of Tables

## References

[1] E.K. Anderson, M. Kamińska, K.C. Chartkunchand, G. Eklund, M. Gatchell, K. Hansen, H. Zettergren, H. Cederquist, and H.T. Schmidt: *Decays of excited silver-cluster anions $Ag_n$, $n = 4$ to 7, in the Double ElectroStatic Ion Ring ExpEriment.* Physical Review A, 98(2):022705, 2018.

[2] K. Blaum, K. Haberkorn, and S. George: *VORLESUNG: STORED CHARGED PARTICLES*. Heidelberg, winter semester 2017/18.

[3] P.T. Boggs, R.H. Byrd, J.E. Rogers, and R.B. Schnabel: *User's reference guide for ODRPACK version 2.01 software for weighted orthogonal distance regression.* 1992.

[4] C. Braams: *Edge effect in charged-particle analyzing magnets.* Nuclear Instruments and Methods, 26:83–89, 1964.

[5] C. Breitenfeldt, K. Blaum, S. George, J. Göck, G. Guzmán-Ramírez, J. Karthein, T. Kolling, M. Lange, S. Menk, C. Meyer, J. Mohrbach, G. Niedner-Schatteburg, D. Schwalm, L. Schweikhard, and A. Wolf: *Long-term monitoring of the internal energy distribution of isolated cluster systems.* Physical Review Letters, 120(25):253001, 2018.

[6] P. Brimblecombe: *Air composition and chemistry.* Cambridge University Press, 1996.

[7] K.C. Chartkunchand, M. Kamińska, E.K. Anderson, M.K. Kristiansson, G. Eklund, O.M. Hole, R.F. Nascimento, M. Blom, M. Björkhage, A. Källberg, P. Löfgren, P. Reinhed, S. Rosén, A. Simonsson, R.D. Thomas, S. Mannervik, V.T. Davis, P.A. Neill, J.S. Thompson, D. Hanstorp, H. Zettergren, H. Cederquist, and H.T. Schmidt: *Radiative lifetimes of the bound excited states of $Pt^-$*. Physical Review A, 94(3):032501, 2016.

[8] W. Demtröder: *Experimentalphysik 3.* Springer Spektrum, Berlin, Heidelberg, 5. aufl. 2016 ed., 2016.

[9] W. Demtröder: *Experimentalphysik 2.* Springer Spektrum, Berlin, Heidelberg, 7. aufl. 2017 ed., 2017.

[10] M. Dole, L.L. Mack, R.L. Hines, R.C. Mobley, L.D. Ferguson, and M.B. Alice: *Molecular beams of macroions.* The Journal of Chemical Physics, 49(5):2240–2249, 1968.

[11] R.C. Dunbar: *BIRD (blackbody infrared radiative dissociation): evolution, principles, and applications.* Mass spectrometry reviews, 23(2):127–158, 2004.

[12] J. Göck: *A new $C_{60}$ ion source for the LIVE project and the auto-fragmentation process of cobalt dimer anions in the Cryogenic Storage Ring CSR.* Master thesis, 2015.

[13] M. Grieser: *private communications*. 2018.

[14] J.H. Gross: *Mass spectrometry: a textbook*. Springer Science & Business Media, 2006.

[15] F. Grussie: *private communications*. 2018.

[16] R. von Hahn, A. Becker, F. Berg, K. Blaum, C. Breitenfeldt, H. Fadil, F. Fellenberger, M. Froese, S. George, J. Göck, M. Grieser, F. Grussie, E.A. Guerin, O. Heber, P. Herwig, J. Karthein, C. Krantz, H. Kreckel, M. Lange, F. Laux, S. Lohmann, S. Menk, C. Meyer, P.M. Mishra, O. Novotný, A.P. O'Connor, D.A. Orlov, M.L. Rappaport, R. Repnow, S. Saurabh, S. Schippers, C.D. Schröter, D. Schwalm, L. Schweikhard, T. Sieber, A. Shornikov, K. Spruck, S. Sunil Kumar, J. Ullrich, X. Urbain, S. Vogel, P. Wilhelm, A. Wolf, and D. Zajfman: *The cryogenic storage ring CSR*. Review of Scientific Instruments, 87(6):063115, 2016.

[17] K. Hansen, M.H. Stockett, M. Kaminska, R.F. Nascimento, E.K. Anderson, M. Gatchell, K.C. Chartkunchand, G. Eklund, H. Zettergren, H.T. Schmidt, and H. Cederquist: *Spontaneous decay of small copper-cluster anions $Cu_n^-$ ($n$ = 3–6), on long time scales*. Physical Review A, 95(2):022511, 2017.

[18] E. Heinicke and H. Baumann: *Penning ion source for MP accelerator*. Nuclear Instruments and Methods, 74(2):229–232, 1969.

[19] F. Hinterberger: *Physik der Teilchenbeschleuniger und Ionenoptik*. Springer-Verlag, 2008.

[20] D.R. Lide: *CRC handbook of chemistry and physics: a ready-reference book of chemical and physical data*. CRC press, 1995.

[21] J. Meija, T.B. Coplen, M. Berglund, W.A. Brand, P. De Bièvre, M. Gröning, N.E. Holden, J. Irrgeher, R.D. Loss, T. Walczyk, and T. Prohaska: *Isotopic compositions of the elements 2013 (IUPAC technical Report)*. Pure and Applied Chemistry, 88(3):293–306, 2016.

[22] S. Menk, P. Bertier, Y. Enomoto, T. Masunaga, T. Majima, Y. Nakano, and T. Azuma: *A cryogenic linear ion trap beamline for providing keV ion bunches*. Review of Scientific Instruments, 89(11):113110, 2018.

[23] C. Meyer, A. Becker, K. Blaum, C. Breitenfeldt, S. George, J. Göck, M. Grieser, F. Grussie, E.A. Guerin, R. von Hahn, P. Herwig, C. Krantz, H. Kreckel, J. Lion, S. Lohmann, P.M. Mishra, O. Novotný, A.P. O'Connor, R. Repnow, S. Saurabh, D. Schwalm, L. Schweikhard, K. Spruck, S. Sunil Kumar, S. Vogel, and A. Wolf: *Radiative rotational lifetimes and state-resolved relative detachment cross sections from photodetachment thermometry of molecular anions in a cryogenic storage ring.* Physical Review Letters, 119(2):023202, 2017.

[24] J. Meyer: *INBETRIEBNAHME EINER LASERVERDAMPFUNGSQUELLE MIT „PICK-UP"-EINHEIT & REAKTIONEN KATIONISCHER TANTALCLUSTER MIT KLEINEN KOHLENWASSERSTOFFEN.* Diploma Thesis, 2009.

[25] R. Middleton: *A versatile high intensity negative ion source.* Nuclear Instruments and Methods in Physics Research, 214(2-3):139–150, 1983.

[26] R. Middleton: *A negative ion cookbook.* University of Pennsylvania, 1989.

[27] P.M. Mishra, K. Blaum, C. Breitenfeldt, S. George, J. Göck, M. Grieser, R. von Hahn, J. Karthein, T. Kolling, C. Krantz, H. Kreckel, S. Kumar, J. Mohrbach, G. Niedner-Schatteburg, C. Meyer, R. Repnow, L. Schweikard, and A. Wolf: *An ion source platform of the cryogenic storage ring (CSR).* Journal of Physics: Conference Series, 635(11):112061, 2015.

[28] Y. Nakano, Y. Enomoto, T. Masunaga, S. Menk, P. Bertier, and T. Azuma: *Design and commissioning of the RIKEN cryogenic electrostatic ring (RICE).* Review of Scientific Instruments, 88(3):033110, 2017.

[29] F. Nuesslein, K. Blaum, S. George, J. Göck, M. Klein, T. Kolling, M. Lembach, G. Niedner-Schatteburg, C. Meyer, P. Mishra, V. Schmidt, R. von Hahn, and A. Wolf: *Collaboration: A new Laser VAPorization (LVAP) source for cluster ion production at the CSR facility.* 2018.

[30] A.P. O'Connor, A. Becker, K. Blaum, C. Breitenfeldt, S. George, J. Göck, M. Grieser, F. Grussie, E.A. Guerin, R. von Hahn, U. Hechtfischer, P. Herwig, J. Karthein, C. Krantz, H. Kreckel, S. Lohmann, C. Meyer, P.M. Mishra, O. Novotný, R. Repnow, S. Saurabh, D. Schwalm, K. Spruck, S. Sunil Kumar, S. Vogel, and A. Wolf: *Photodissociation of an Internally Cold Beam of $CH^+$ Ions in a Cryogenic Storage Ring.* Physical Review Letters, 116(11):113002, 2016.

[31] I. Rahinov, Y. Toker, K. Hansen, D. Schwalm, O. Heber, and D. Zajfman: *Effect of a localized charge on the stability of Van der Waals clusters.* The European Physical Journal D, 70(12):260, 2016.

[32] R. Repnow: *private communications*. 2018.

[33] H.T. Schmidt, G. Eklund, K.C. Chartkunchand, E.K. Anderson, M. Kamińska, N. de Ruette, R.D. Thomas, M.K. Kristiansson, M. Gatchell, P. Reinhed, S. Rosén, A. Simonsson, A. Källberg, P. Löfgren, S. Mannervik, H. Zettergren, and H. Cederquist: *Rotationally Cold $OH^-$ Ions in the Cryogenic Electrostatic Ion-Beam Storage Ring DESIREE.* Physical Review Letters, 119(7):073001, 2017. Erratum: Phys. Rev. Lett 121, 079901, 2018.

[34] H.T. Schmidt, R.D. Thomas, M. Gatchell, S. Rosén, P. Reinhed, P. Löfgren, L. Brännholm, M. Blom, M. Björkhage, E. Bäckström, J.D. Alexander, S. Leontein, D. Hanstorp, H. Zettergren, L. Liljeby, A. Källberg, A. Simonsson, F. Hellberg, S. Mannervik, M. Larsson, W.D. Geppert, K.G. Rensfelt, H. Danared, A. Paál, M. Masuda, P. Halldén, G. Andler, M.H. Stockett, T. Chen, G. Källersjö, J. Weimer, K. Hansen, H. Hartman, and H. Cederquist: *First storage of ion beams in the Double Electrostatic Ion-Ring Experiment: DESIREE.* Review of Scientific Instruments, 84(5):055115, 2013.

[35] V. Schmidt: *Design of an ion beam extraction optics and analysis of the molecular composition of an ion beam in an electrostatic storage ring.* Bachelor thesis, 2018.

[36] V. Schmidt: *private communications*. 2018.

[37] Y. Toker, I. Rahinov, D. Schwalm, U. Even, O. Heber, M. Rappaport, D. Strasser, and D. Zajfman: *Blackbody-induced radiative dissociation of cationic $SF_6$ clusters.* Physical Review A, 86(2):023202, 2012.

[38] B. Wolf: *Handbook of Ion Sources.* CRC Press, 1995.

## Danksagung

An dieser Stelle möchte ich mich bei allen bedanken, die zum Gelingen dieser Arbeit und dieses Projektes beigetragen haben. Ich danke ...

... Prof. Dr. Andreas Wolf für die Möglichkeit, dieses Projekt durchführen zu dürfen und für die Betreuung und die Kommentare auf dem Weg zur fertigen Arbeit.

... Priv.-Doz. Dr. Robert Moshammer für die freundliche Bereiterklärung, diese Arbeit zu begutachten.

... Prof. Dr. Klaus Blaum für die Möglichkeit, diese Arbeit am MPIK anfertigen zu dürfen.

... Prof. Dr. Gereon Niedner-Schatteburg, Dr. Thomas Kolling, Michael Lembach und Matthias Klein für die Einblicke zur Funktionsweise der Laserverdampfungsquelle in Kaiserslautern und die Möglichkeit zur Durchführung des Kollaborationsprojektes über eine Laserverdampfungsquelle für den CSR.

... Dr. Sebastian George für die Betreuung und Unterstützung dieses Projektes.

... Dr. Christian Meyer für die Betreuung dieses Projektes, die vielen fachlichen und über das Fachliche hinausgehenden Gespräche und Diskussionen, die Kommentare und Ratschläge zu meiner Arbeit und die regelmäßige gegenseitige Kaffeezufuhr.

... Jürgen Göck für die interessanten physikalischen und nichtphysikalischen Gespräche und die Ratschläge zu diesem Projekt.

... Viviane Schmidt für die Simulationen zur elektrostatischen Ionenoptik, die fachlichen und nichtfachlichen Gespräche und die abzählbar unendliche Menge an Muffins und Kuchen.

... Dr. Florian Grussie für die Unterstützung bei der Simulation des Magneten.

... Dr. Manfred Grieser für die Ratschläge zur Simulation des Magneten.

... Dr. Robert von Hahn und Dr. Roland Repnow für die Unterstützung bei der Realisierung des experimentellen Aufbaus.

... Dr. Holger Kreckel für die freundliche Zurverfügungstellung einiger Messgeräte.

... Dr. Preeti Mishra für die Unterstützung bei der Bestellung einiger Komponenten.

... Rolf Epking, Manfred König, Max Trebis, Karsten Stähle und Dietmar Hübner für die technische Unterstützung bei der Realisierung des experimentellen Aufbaus.

... Thorsten Spranz, Frank Müller und Peter Gahn für die Konstruktion und Fertigung vieler Teile des experimentellen Aufbaus.

... Dirk Kaiser, Christian Kaiser und Steffen Vogel für die mechanische Unterstützung bei der Realisierung des experimentellen Aufbaus.

... meinen Freunden, die ich während meiner Studienzeit in Heidelberg kennengelernt habe, für die unvergessliche Zeit.

... meiner Familie und meinen Freunden in der Heimat für ihre jahrelange, uneingeschränkte Unterstützung.

## Erklärung

Ich versichere, dass ich diese Arbeit selbstständig verfasst habe und keine anderen als die angegebenen Quellen und Hilfsmittel benutzt habe.

Heidelberg, den 06.12.2018 .....